Applied Ocean Research 172 (2026) 105120

Contents lists available at ScienceDirect

Applied Ocean Research

journal homepage: www.elsevier.com/locate/apor

Research paper

Inertia-driven wave energy converter for Marine buoy power supply: motion response and energy conversion characteristics

Xiongbo Zheng [a,*], Wenbin Lai [a], Jialong Li [a], Fengmei Jing [b], Sizhang Rong [a], Lin Cui [c], Hongkun Yang [a]

[a] *School of Mathematics Science, Harbin Engineering University, Harbin 150001, China*
[b] *School of Mechanical Engineering, Beijing Institute of Technology, Beijing 100081, China*
[c] *National Ocean Technology Center, Tianjin 300112, China*

ARTICLE INFO

Keywords:
Wave energy converter
Marine buoy
Motion response
Power generation performance
Daily power generation

ABSTRACT

Marine buoys operating in deep-sea environments frequently face power shortages, necessitating the urgent development of new power supply solutions to meet their increasing energy demands. This study proposes an Inertia-Driven Wave Energy Converter (IDWEC) that utilizes the motion of a sliding body to drive a generator for electricity production. The paper investigates the motion response and energy conversion characteristics of the IDWEC-buoy integrated system. Firstly, a mathematical model for the energy conversion of the integrated system under both regular and irregular waves is established. Subsequently, the Boundary Element Method (BEM) is employed to analyze the effects of wave period, power take-off (PTO) damping, spring stiffness, the horizontal distance between the centers of gravity of the IDWEC and the buoy, and wave direction on the system performance. A physical model of the IDWEC-buoy integrated system is constructed, and wave tank tests are conducted to validate the reliability of the numerical results. Finally, based on the 2022 South China Sea wave scatter diagram, the daily average power generation of the IDWEC under real-sea wave conditions is estimated. Research results indicate that the IDWEC-buoy integrated system exhibits three distinct resonant frequencies. The resonant frequency can be adjusted by varying the mass of the sliding body or the spring stiffness, enabling matching with the wave conditions in the target sea area to enhance power output. When the sliding mass is small, the optimal spring stiffness approximately satisfies $\omega^2 m$. Under optimal spring stiffness, maximum power output occurs when the relative displacement amplitude of the sliding body equals precisely half the stroke length (L/2). The daily average power generation of the IDWEC under South China Sea random wave conditions is predicted to be 455.92 Wh, which meets the daily energy consumption requirements of the sensors on the buoy. This work confirms that the IDWEC can provide an efficient and sustainable power solution for buoys.

1. Introduction

Covering over 70% of the Earth's surface, the ocean plays a pivotal role as both a global climate regulator and a carbon cycle mediator, and harbors abundant resources along with vast unexplored territories (DeVries, 2022; Isson et al., 2020; Martínez et al., 2021). Long-term environmental monitoring and scientific investigations in marine ecosystems hold significant strategic and scientific value (Danovaro et al., 2020; Zhivkoplias et al., 2024). As the marine economy expands from coastal regions to deep-sea environments (Felski and Zwolak, 2020; Hein et al., 2020), various marine buoys (Aguzzi et al., 2019; García et al., 2018) have emerged as crucial research platforms. These buoy systems typically integrate multiple sensors that require substantial power supplies, making reliable power generation fundamental to their sustained operation in marine environments. However, deep-sea deployment poses formidable challenges for power systems. The harsh operational conditions and remote locations render conventional cable-based power transmission impractical or infeasible. Current energy solutions for marine buoys primarily rely on fuel-powered generators or chemical batteries (Pan et al., 2021; Wang, 2015), yet such conventional approaches exhibit three critical limitations: restricted service life, substantial maintenance expenses, and the environmental hazards inherent in fossil fuel dependence. These challenges underscore the urgent need for innovative power supply systems to ensure the

---

* Corresponding author at: School of Mathematics Science, Harbin Engineering University, Haerbin, Heilongjiang, China.
E-mail address: zhengxiongbo@hrbeu.edu.cn (X. Zheng).

https://doi.org/10.1016/j.apor.2026.105120
Received 10 March 2025; Received in revised form 28 March 2026; Accepted 27 May 2026

long-term stability and sustainability of deep-sea marine buoy operations (Shi et al., 2017; Wu et al., 2015; Xi et al., 2019).

The ocean harbors abundant energy resources, including solar, wind, wave, and tidal energy. Compared to solar and wind energy, wave energy demonstrates distinct advantages such as broader spatial distribution, higher energy density, and reduced susceptibility to temperature fluctuations and climatic variations (Astariz and Iglesias, 2015; Azam et al., 2024; Zheng et al., 2017). These characteristics make it particularly suitable as a supplementary power source for marine buoy operating in deep-sea environments. A key advantage of WECs lies in their ability to generate pollution-free and sustainable electricity without consuming chemical fuels. Currently, WECs are typically categorized into Oscillating Water Column (OWC), Oscillating Buoy (OB), and overtopping systems, and are predominantly used for powering large-scale marine equipment (Di Lauro et al., 2020; Lai et al., 2025; Zheng et al., 2020). For small and medium-sized marine buoys, however, the aforementioned WECs may be too bulky and costly. Currently, research on small and medium-sized WECs is relatively limited. According to statistics from the incoPat patent database (Yue et al., 2025), the United States was the first to apply for patents related to using wave energy to power marine buoys. As of 2021, the U.S., South Korea, and China had submitted a total of eight patents in this field, with the U.S. and South Korea each holding three and China holding two. Available WECs targeting small and medium-sized marine buoys are mainly divided into internal and external types. External WECs directly contact waves, enabling more efficient absorption of wave energy. Based on buoy shape characteristics, external WECs can be further classified into turbine-type, spherical-type, nodding duck-type, and blade-type, among others (Hwang et al., 2016; Joe et al., 2017; Wang et al., 2015; Wen et al., 2016). However, due to direct exposure to seawater, external WECs exhibit poor corrosion resistance, resulting in lower operational reliability. Internal WECs are installed inside the buoy, collecting vibrational energy generated by the buoy's heaving (vertical motion) or pitching (rotational motion) induced by waves. This design avoids direct contact with waves, preventing seawater corrosion and thereby extending the WEC’s service life. Compared to external WECs, internal WECs are more suitable for marine buoys. Nevertheless, internal WECs also face significant challenges, including limited power generation capacity, high manufacturing costs, and poor operational stability, which currently hinder their widespread adoption.

Zheng et al. (2022) proposed an external oscillating-body wave energy converter (OBWEC), in which the oscillating body is mounted to the outer wall of a buoy via a support frame, as shown in Fig. 1(a). It utilizes the heave motion of the oscillating body under wave action to drive the PTO system for power generation. Their results indicate that the minimum starting wave height for this OBWEC under real sea conditions is 0.3 m. Xu et al. (2022) integrated a buoy with an OWC, proposing two internal-type WECs, illustrated in Fig. 1(b). Huang et al. (2021) proposed a pendulum-type WEC with a hydraulic PTO system, connected to a buoy via a hinge joint, depicted in Fig. 1(c). They found that selecting an appropriate PTO damping coefficient is crucial for improving the WEC's performance, and that this device demonstrates good wave energy capture capability within a certain wave range. Cordonnier Cordonnier et al. (2015) developed the SEAREV WEC, which consists of a sealed floating platform housing an internal heavy swinging pendulum. Research shows that it achieves effective energy conversion under open-ocean conditions, although its performance is significantly affected by wave direction. Cheng et al. (2022) conducted a performance comparison between the OB-type WEC and the OWC-type WEC, and verified the results through physical model experiments. Their findings revealed that the OWC-type WEC configuration exhibits superior wave energy extraction performance. Similar studies can be found

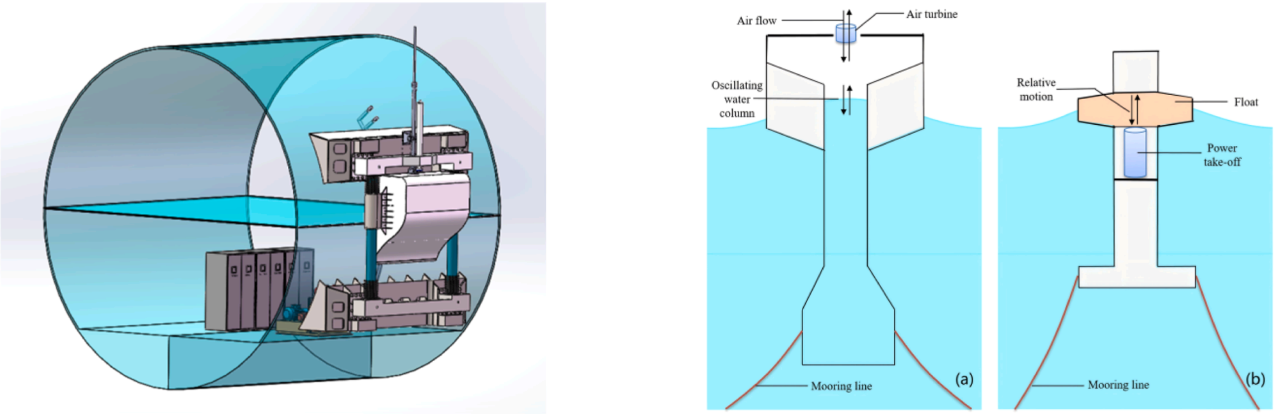

(a) External-type OBWEC [26].

(b) Internal-type WEC [27].

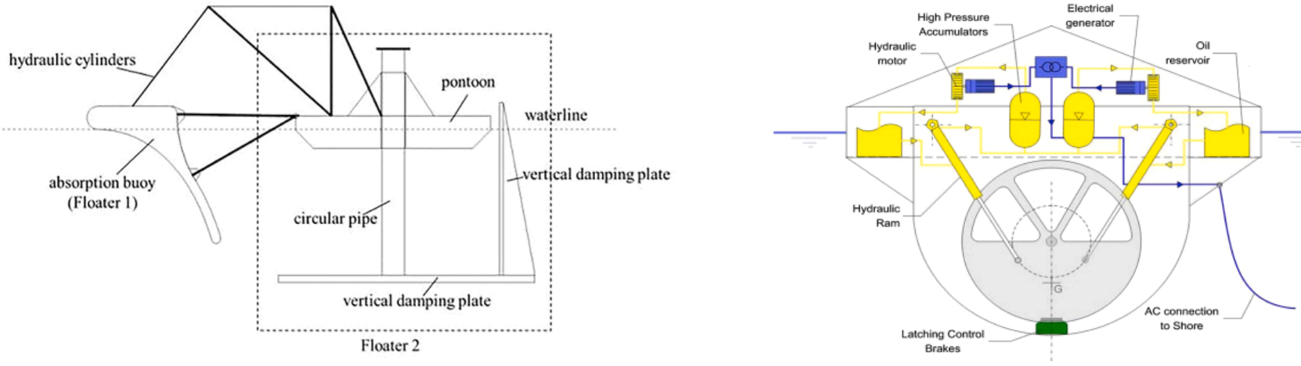

(c) Pendulum-type WEC [28].

(d) SEAREV WEC [29].

Fig. 1. Several different types of WEC power the buoy.

in (Cheng et al., 2022; Cheng et al., 2024; Cheng et al., 2024).

As commercial activities in the deep sea increase, marine buoys face growing demand for greater stability and efficiency in their energy supply. This underscores the need to upgrade small-scale wave energy converters (WECs) designed for such buoys. To address persistent power supply challenges in these buoys operating in deep-sea environments, this paper proposes a novel IDWEC featuring a compact structure and lightweight design that can be integrated into marine buoys. The system supports the combined power output of multiple IDWEC units without motion interference, utilizing the motion of an internal sliding body to drive a generator for electricity production.

The structure of this paper is organized as follows. Section 2 describes the working principles and main structural dimensions of the IDWEC-buoy integrated system, and establishes the mathematical model for its energy conversion. Sections 3 and 4 systematically investigate the effects of various parameters on the motion response and power generation performance of the IDWEC using the boundary element method. Section 5 presents the physical models of the IDWEC and buoy, validates the numerical results, and examines the influence of external electrical loads, spring stiffness, and sliding body mass on the motion responses and power output of the IDWEC. Section 6 analyzes the motion response and energy conversion characteristics of the integrated system under random wave conditions, and predicts the daily average power generation of the IDWEC under random wave conditions in the South China Sea area. Finally, Section 7 presents the conclusions.

2. Introduction of the IDWEC and its working principle integrated with a buoy

This section provides a detailed introduction to the structure and component systems of the IDWEC, as well as the mathematical model for its energy conversion when integrated with a buoy.

2.1. Structural model of the IDWEC

Fig. 2 illustrates the internal structure of the IDWEC, which comprises three modules: the transmission module (Fig. 2(I)), the inertia module (Fig. 2(II)), and the power generation module (Fig. 2(III)). The transmission module is located in the upper part of the IDWEC and includes components such as guide wheels, stepped pulleys, steel wire ropes, and other connecting components. The inertia module, positioned in the middle part, consists of a sliding body (with adjustable mass parameters), springs (with adjustable stiffness parameters), and guide columns. The power generation module is situated in the lower part and contains a generator, a gearbox, guide wheels, and a controller. The sliding body within the inertia module acts as the energy-capturing component of the IDWEC. It harnesses wave energy transmitted by the buoy and converts it into mechanical energy, which includes the kinetic energy of the sliding body, its gravitational potential energy, and the elastic potential energy of the springs. During its motion, the sliding body drives the generator via the transmission module to produce electricity, thereby completing the conversion from wave energy to electrical energy. A structural schematic of the IDWEC is shown in Fig. 2 (IV), with a spring system installed on each side. The three-dimensional physical model of the IDWEC is presented in Fig. 2(V).

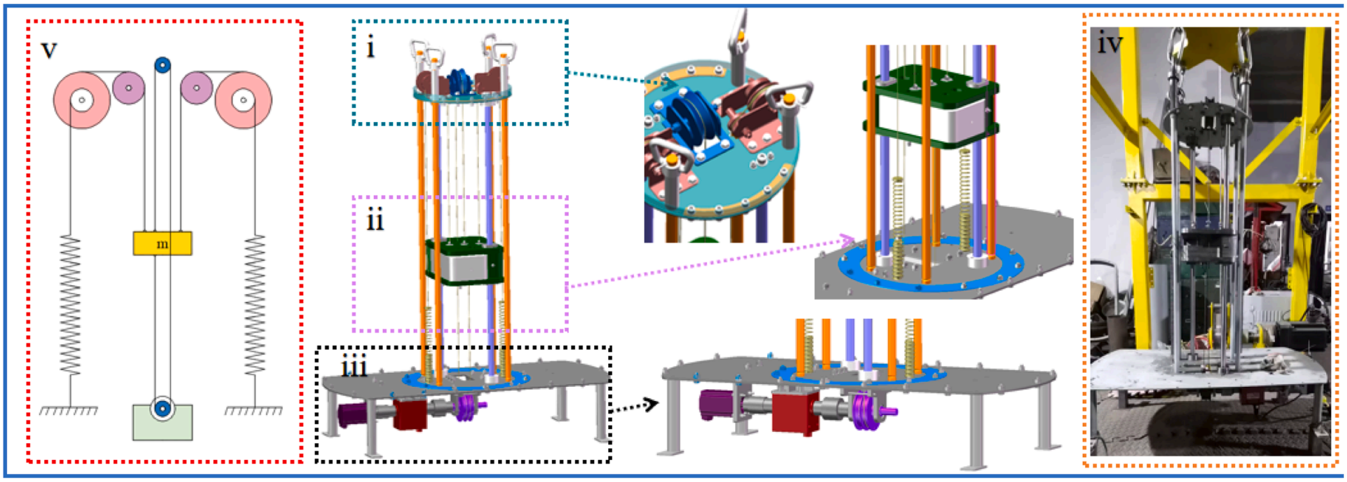

Fig. 2. Internal structure and physical model of the IDWEC.

Fig. 3 is the schematic diagram of the IDWEC integrated with a marine buoy. The IDWEC is fully enclosed within the buoy and isolated from direct seawater contact, significantly enhancing its survivability and ensuring high reliability. The working principle is as follows: the IDWEC moves together with the buoy under wave excitation. When the buoy undergoes pitch or heave motion, inertial forces induce relative motion of the sliding body inside the IDWEC with respect to the buoy. This relative motion is transmitted via a steel wire rope to drive the generator, thereby converting mechanical energy into electricity. To balance the eccentric torque exerted on the buoy by the IDWEC, counterweights of equivalent mass are positioned symmetrically opposite the IDWEC at an equal lever arm. This configuration aligns the center of gravity of the integrated system with the central vertical axis of the buoy. During numerical simulations, *r* is variable, and the position of the counterweight is adjusted accordingly. During wave tank tests, however, the position of the IDWEC is fixed, and therefore the counterweight position remains fixed as well. Fig. 3(b) shows a prototype marine buoy (Wang et al., 2016).

2.2. Mathematical model of energy conversion of the IDWEC-Buoy integrated system

In Fig. 3, since the centers of gravity of the IDWEC and the buoy are not aligned on the same vertical axis, the energy absorption analysis of the IDWEC must consider the pitch response of the buoy. Based on potential flow theory, and assuming the fluid to be irrotational, inviscid, and incompressible, with the PTO system treated as linear, the coupled equations of motion for the IDWEC under monochromatic waves are formulated as follows:

$$\begin{cases} (M-m+A_{33})\ddot{\xi}_3+B_{33}\dot{\xi}_3+C_{33}\xi_3+A_{35}\ddot{\theta}_5+B_{35}\dot{\theta}_5=F_{e3}+F_{PTO} \\ (I_{t5}+A_{55})\ddot{\theta}_5+B_{55}\dot{\theta}_5+C_{55}\theta_5+A_{53}\ddot{\xi}_3+B_{53}\dot{\xi}_3=M_{e5}+F_{PTO}\cdot r \\ m\ddot{\xi}_{i3}-C_{PTO}(\dot{\xi}_3+r\dot{\theta}_5-\dot{\xi}_{i3})-k_{PTO}(\xi_3+r\theta_5-\xi_{i3})=0 \\ F_{PTO}=-C_{PTO}(\dot{\xi}_3+r\dot{\theta}_5-\dot{\xi}_{i3})-k_{PTO}(\xi_3+r\theta_5-\xi_{i3}) \end{cases} \tag{1}$$

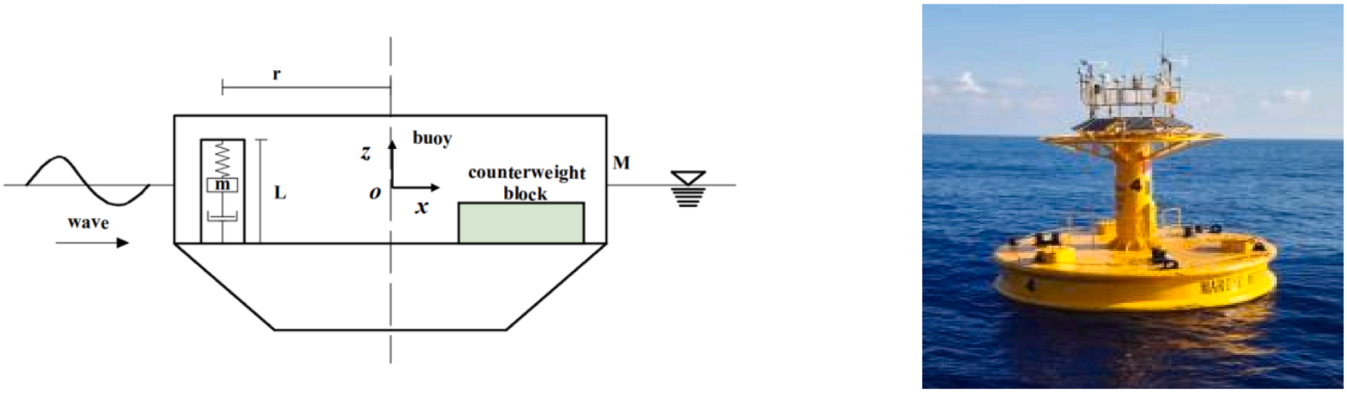

(a) Schematic diagram of the IDWEC integrated with buoy.

(b) A prototype of a marine buoy [34].

Fig. 3. Integrated solution of buoy and IDWEC.

where ξ_3 and θ_5 represent the displacement and angular displacement of the buoy in heave and pitch motions, respectively; ξ_{i3} denotes the absolute displacement of the sliding body; F_{e3} and M_{e5} are the heave excitation force and pitch excitation torque acting on the buoy, respectively; F_{PTO} is the control force applied by the PTO system on the buoy, M is the total mass of the buoy and IDWEC combined, I_{t5} is their combined moment of inertia about the pitch axis, and m is the mass of the sliding body, $A_{35} = A_{53}$, $B_{35} = B_{53}$ represent the added mass and radiation damping, respectively, for the coupled heave-pitch motion of the buoy, while A_{55} and B_{55} denote the added mass and radiation damping coefficients for the pitch motion. C_{33} and C_{55} are the restoring coefficients for the buoy in heave and pitch, respectively, with $C_{33} = \rho g S$ (where S is the waterplane area) and $C_{55} = \rho g h V$ (where ρ is water density, g is gravity, h is transverse metacentric height, V is displaced volume). Finally, r is the lever arm, denoting the horizontal distance between the center of gravity of the IDWEC and that of the buoy.

Eq. (1) can be written in matrix form. First, define the state vector as:

$$X = \begin{bmatrix} \xi_3 \\ \theta_5 \\ \xi_{i3} \end{bmatrix} \quad \dot{X} = \begin{bmatrix} \dot{\xi}_3 \\ \dot{\theta}_5 \\ \dot{\xi}_{i3} \end{bmatrix} \quad \ddot{X} = \begin{bmatrix} \ddot{\xi}_3 \\ \ddot{\theta}_5 \\ \ddot{\xi}_{i3} \end{bmatrix} \quad F = \begin{bmatrix} F_{e3} \\ M_{e5} \\ 0 \end{bmatrix} \tag{2}$$

The matrix form of Eq. (1) can be expressed as:

$$M\ddot{x} + C\dot{x} + Kx = F \tag{3}$$

where the mass matrix M, damping matrix C, and stiffness matrix K are:

$$M = \begin{bmatrix} M - m + A_{33} & A_{35} & 0 \\ A_{53} & I_{t5} + A_{55} & 0 \\ 0 & 0 & m \end{bmatrix}, C = \begin{bmatrix} B_{33} + C_{PTO} & B_{35} + rC_{PTO} & -C_{PTO} \\ B_{53} + C_{PTO}r & B_{55} + r^2 C_{PTO} & -rC_{PTO} \\ -C_{PTO} & -C_{PTO}r & C_{PTO} \end{bmatrix}, K = \begin{bmatrix} C_{33} + k_{PTO} & rk_{PTO} & -k_{PTO} \\ rk_{PTO} & C_{55} + r^2 k_{PTO} & -rk_{PTO} \\ -k_{PTO} & -k_{PTO}r & k_{PTO} \end{bmatrix} \tag{4}$$

The expression for the relative displacement between the sliding body and the buoy is:

$$z_r = \xi_{i3} - \xi_3 - r\theta_5 \tag{5}$$

Assume the system performs harmonic motion in regular waves, all variables can be expressed in the frequency domain as:

$$\xi_3 = \overline{\xi}_3 e^{i\omega t} \; \xi_{i3} = \overline{\xi}_{i3} e^{i\omega t} \; \theta_5 = \overline{\theta}_5 e^{i\omega t} \; F_{e3} = \overline{F}_{e3} e^{i\omega t} \; M_{e5} = \overline{M}_{e5} e^{i\omega t} \tag{6}$$

Then, the amplitude expression of the relative displacement is:

$$\overline{z}_r = \overline{\xi}_{i3} - \overline{\xi}_3 - r\overline{\theta}_5 \tag{7}$$

In the frequency domain, Eq. (3) can be expressed as:

$$\left[-\omega^2 M + i\omega C + K\right] \begin{bmatrix} \overline{\xi}_3 \\ \overline{\theta}_5 \\ \overline{\xi}_{i3} \end{bmatrix} = \begin{bmatrix} \overline{F}_{e3} \\ \overline{M}_{e5} \\ 0 \end{bmatrix} \tag{8}$$

Define the impedance matrix of the system as:

$$Z(\omega) = \left[-\omega^2 M + i\omega C + K\right] = \begin{bmatrix} Z_{11} & Z_{12} & Z_{13} \\ Z_{21} & Z_{22} & Z_{23} \\ Z_{31} & Z_{32} & Z_{33} \end{bmatrix} \tag{9}$$

where the elements are:

$$Z_{11} = -\omega^2 (M - m + A_{33}) + i\omega(B_{33} + C_{PTO}) + (C_{33} + k_{PTO})$$

$$Z_{12} = -\omega^2 A_{35} + i\omega(B_{35} + rC_{PTO}) + rk_{PTO}$$

$$Z_{13} = -i\omega C_{PTO} - k_{PTO}$$

$$Z_{21} = -\omega^2 A_{53} + i\omega(B_{53} + C_{PTO}r) + rk_{PTO}$$

$$Z_{22} = -\omega^2 (I_{t5} + A_{55}) + i\omega\left(B_{55} + r^2 C_{PTO}\right) + \left(B_{55} + r^2 C_{PTO}\right)$$

$$Z_{23} = -i\omega rC_{PTO} - k_{PTO}r$$

$$Z_{31} = -i\omega C_{PTO} - k_{PTO}$$

$$Z_{32} = -i\omega C_{PTO}r - k_{PTO}r$$

$$Z_{33} = -\omega^2 m + i\omega C_{PTO} + k_{PTO}$$

Therefore, the amplitude of relative displacement can be written as:

$$\overline{z}_r(\omega) = \frac{1}{\det\,[Z]} \left[(H_{11} + rH_{21} - H_{31})\overline{F}_{e3} + (H_{12} + rH_{22} - H_{32})\overline{M}_{e5}\right] \tag{10}$$

where, det [Z] is the determinant of the impedance matrix, and H_{ij} are the cofactors corresponding to elements of the adjugate matrix, specifically: $\det[\mathrm{Z}] = Z_{11}(Z_{22}Z_{33} - Z_{23}Z_{32}) - Z_{12}(Z_{21}Z_{33} - Z_{23}Z_{31}) + Z_{13}(Z_{21}Z_{32} - Z_{22}Z_{31})$, $H_{11} = Z_{22}Z_{33} - Z_{23}Z_{32}$, $H_{12} = Z_{23}Z_{31} - Z_{21}Z_{33}$, $H_{21} = Z_{13}Z_{32} - Z_{12}Z_{33}$, $H_{22} = Z_{11}Z_{33} - Z_{13}Z_{31}$, $H_{31} = Z_{12}Z_{23} - Z_{13}Z_{22}$, $H_{32} = Z_{13}Z_{21} - Z_{11}Z_{23}$.

The excitation force and torque are related to wave amplitude A by $\overline{F}_{e3} = f_{e3}(\omega)A$ and $\overline{M}_{e5} = m_{e5}(\omega)A$, where $f_{e3}(\omega)$ and $m_{e5}(\omega)$ are the transfer functions of the heave excitation force and pitch excitation torque, respectively.

Therefore, the Response Amplitude Operator (RAO) of the relative displacement can be expressed as:

$$RAO_{\overline{z}_r}(\omega) = \frac{|\overline{z}_r(\omega)|}{A} = \frac{1}{\det[\mathrm{Z}]}\left[(H_{11} + rH_{21} - H_{31})f_{e3}(\omega) + (H_{12} + rH_{22}1H_{32})m_{e5}(\omega)\right] \tag{11}$$

Similarly, the RAO for heave and pitch motions of the buoy are respectively:

$$RAO_{\xi_3}(\omega) = \left|\frac{1}{\det[\mathrm{Z}]}\left[(Z_{22}Z_{33} - Z_{23}Z_{32})f_{e3}(\omega) - (Z_{12}Z_{33} - Z_{13}Z_{32})m_{e5}(\omega)\right]\right| \tag{12}$$

$$RAO_{\theta_5}(\omega) = \left|\frac{1}{\det[\mathrm{Z}]}\left[(Z_{23}Z_{31} - Z_{21}Z_{33})f_{e3}(\omega) + (Z_{11}Z_{33} - Z_{13}Z_{31})m_{e5}(\omega)\right]\right| \tag{13}$$

The average output power of IDWEC can be expressed as:

$$P_{ave}(\omega) = \frac{1}{2}\cdot C_{PTO}\omega^2|\overline{z}_r|^2 = \frac{1}{2}\cdot C_{PTO}\omega^2\left|\frac{1}{\det[\mathrm{Z}]}\left[(H_{11} + rH_{21} - H_{31})f_{e3}(\omega) + (H_{12} + rH_{22}1H_{32})m_{e5}(\omega)\right]\right|^2 A^2 \tag{14}$$

For regular waves, the average wave energy power per unit width in deep water is (Thiruvenkatasamy and Neelamani, 1997):

$$P_{re} = \frac{\rho g^2 H^2 T}{32\pi} \tag{15}$$

where, H is the wave height, T is the wave period.

In real seas, waves are typically random. A common approach to handling random waves is to decompose them into regular wave components whose amplitudes are determined by a discrete wave spectrum. The standard JONSWAP spectrum is one of the most commonly used wave spectra and is defined as (Deng et al., 2023):

$$S(\omega) = 0.204H_s^2\frac{\omega_p^4}{\omega^5}\exp\left[-\frac{5}{4}\left(\frac{\omega_p}{\omega}\right)^4\right]3.3^{exp\left[-\frac{(\omega-\omega_p)^2}{2\sigma^2\omega_p^2}\right]} \tag{16}$$

where $\sigma = 0.07$ when $\omega \le \omega_p$, and $\sigma = 0.09$ when $\omega > \omega_p$, ω_p is the peak frequency and H_s is the significant wave height.

For the $n - th$ discretized regular-wave component with the frequency ω_i, the wave amplitude is

$$a_i = \sqrt{2S(\omega_n)\Delta\omega} \tag{17}$$

where $\Delta\omega$ is the sampling interval of the discretized frequency. The time-average absorbed power of the IDWEC in random waves is equal to the sum of the absorbed power at each discrete wave frequency, that is:

$$\overline{P} = \sum_n P_n \tag{18}$$

where

$$P_n = \frac{1}{2}\cdot C_{PTO}\omega^2|\overline{z}(\omega_n)|^2 \tag{19}$$

For irregular waves, the average wave energy power per unit width in deep water can be expressed as:

$$P_{ir} = \frac{\rho g^2 H_s^2 T_e}{64\pi} \tag{20}$$

where, H_s is the significant wave height, T_e is the energy Period ($T_e \approx 0.9T_p$), and T_p is the peak period.

The power generation efficiency of IDWEC can be expressed as:

$$\eta_w = \frac{P_e}{P_{re}/P_{ir} * D}\cdot 100\% \tag{21}$$

where, D is the width of the buoy, $D = 2.5$m.

2.3. Verification of the mathematical model

Table 1 presents the basic parameters of the buoy. The total mass of the buoy is 1660 kg, its moment of inertia about the RY-axis is 724.33 kg·m^2, and its waterplane area is 4.902 m^2.

Fig. 4 presents the RAOs of the buoy for heave and pitch motions, obtained from Eqs. (12) and (13), respectively, compared with AQWA results. The results exhibit good agreement, effectively validating the reliability of the mathematical model established in Section 2.2.

3. Coupling response characteristics of the integrated system

This section analyzes the motion response and energy conversion characteristics of the buoy-IDWEC integrated system under various

Table 1
Basic parameters of the buoy.

Parameter	Unit	Value	Parameter	Unit	Value
Diameter of the buoy	m	2.5	Total moment of inertia	kg.m^2	724.33
Mass of the buoy	kg	1660	Displacement of the buoy	m^3	1.623
Buoy draft	mm	900	Waterplane area of the buoy	m^2	4.902

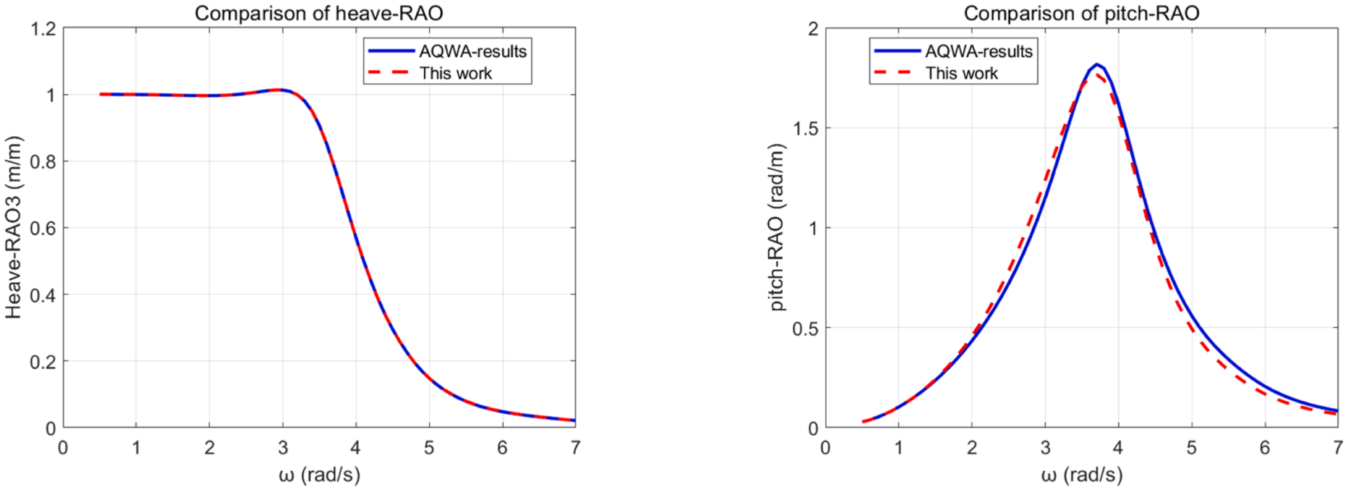

(a) heave RAO

(b) pitch RAO

Fig. 4. Comparison of RAO between AQWA and this work.

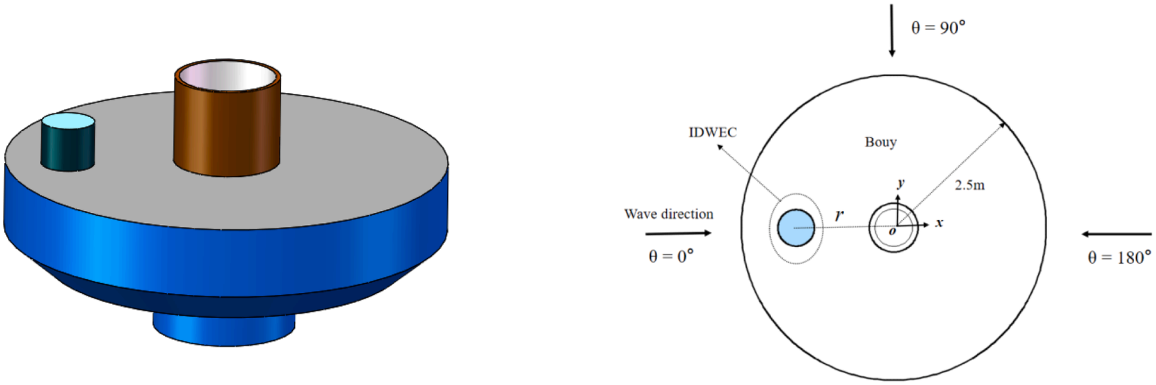

(a) 2.5-meter-diameter marine buoy

(b) Layout diagram of the IDWEC within integrated system

Fig. 5. 3D model integrated with IDWEC and buoy.

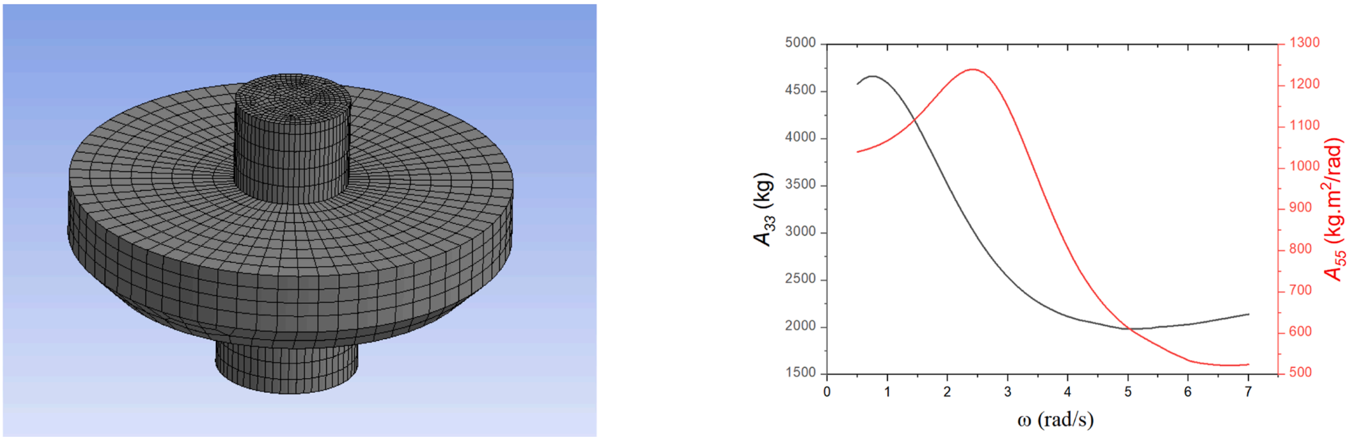

(a). Mesh model	(b). Added mass

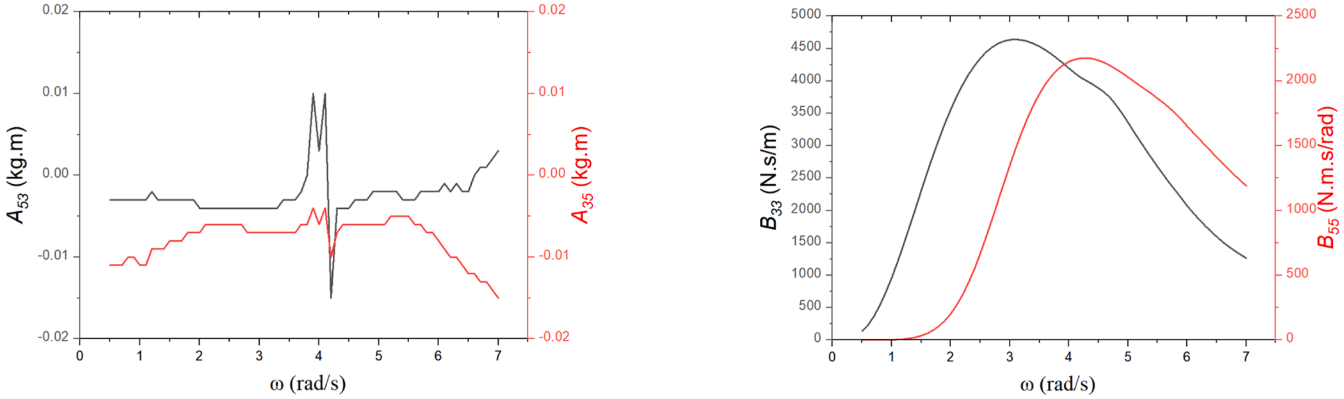

(c). Coupling additional mass	(d). Radiation damping

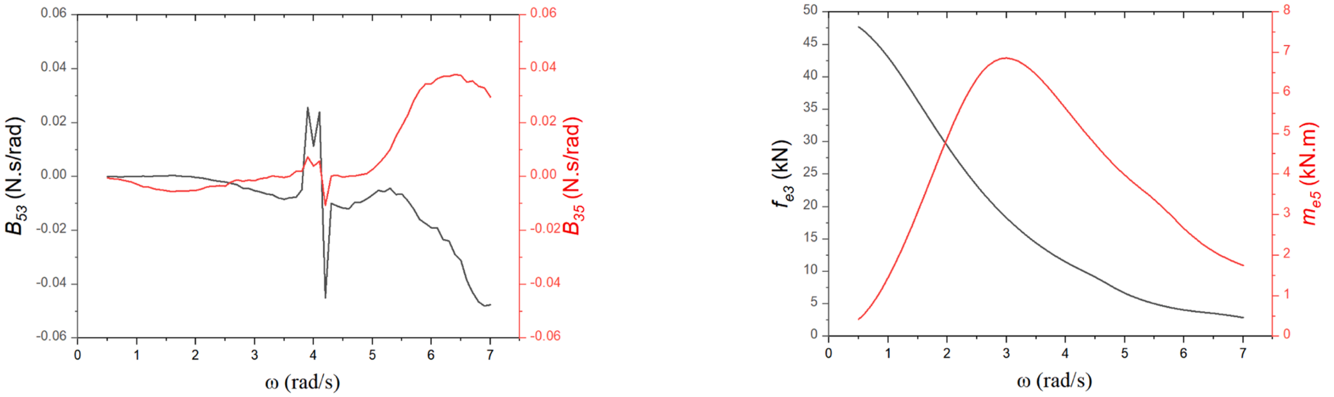

(c). Coupling radiation damping	(f). Excitation force phaseand

Fig. 6. Hydrodynamic parameters of buoy in heave and pitch motions.

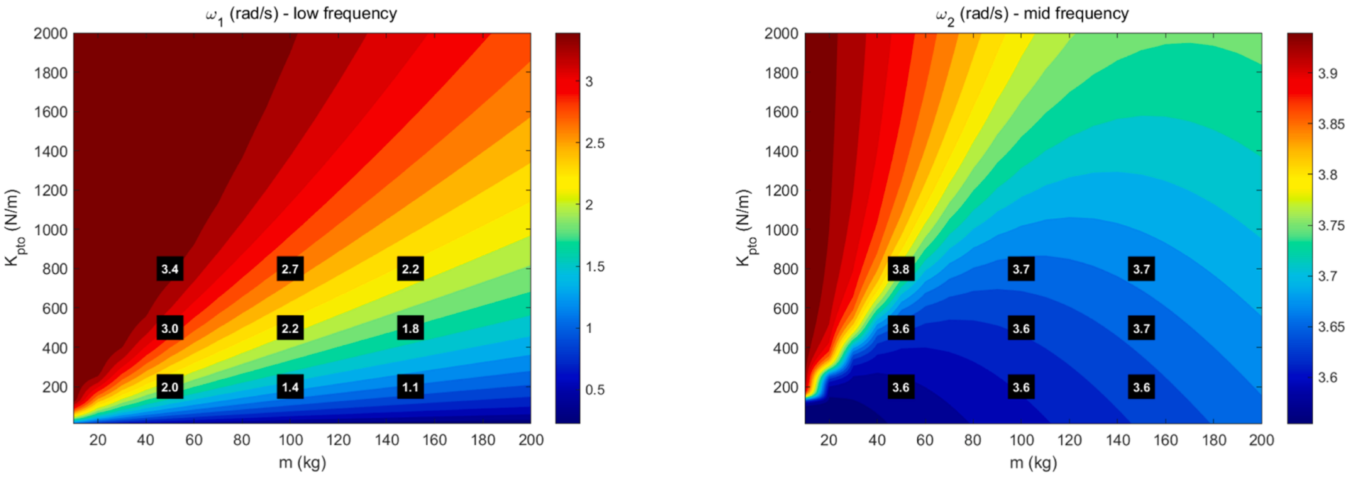

(a). First resonant frequency

(b). Second resonant frequency,

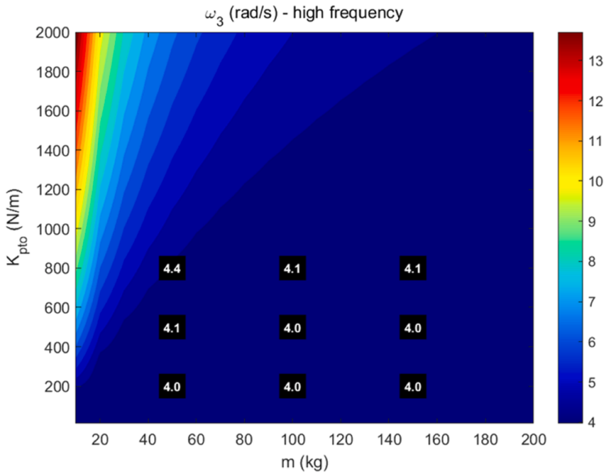

(c). Third resonant frequency

Fig. 7. Cloud map of the resonant frequency for variable m and k_{PTO}.

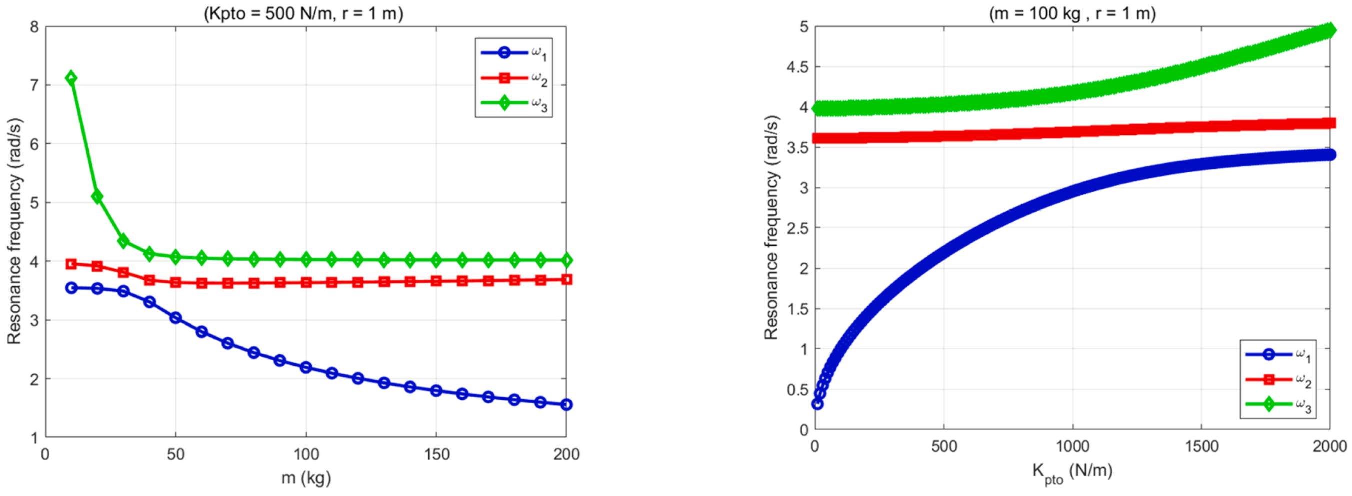

(a). Variable m

(b). Variable k_{PTO}

Fig. 8. Resonance frequency under varying m or k_{PTO}.

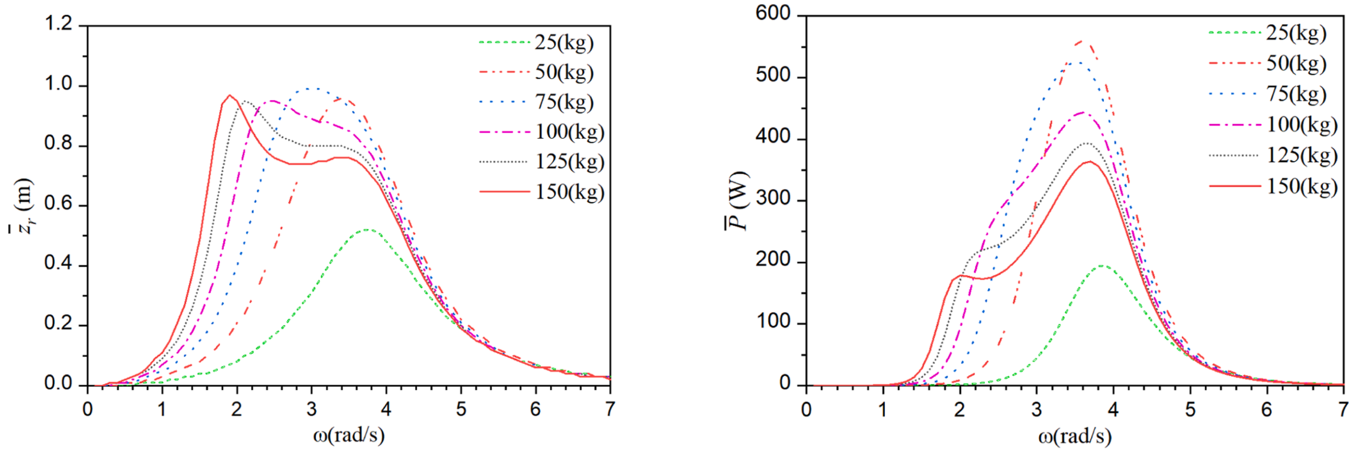

(a). Relative displacement

(b). Average power

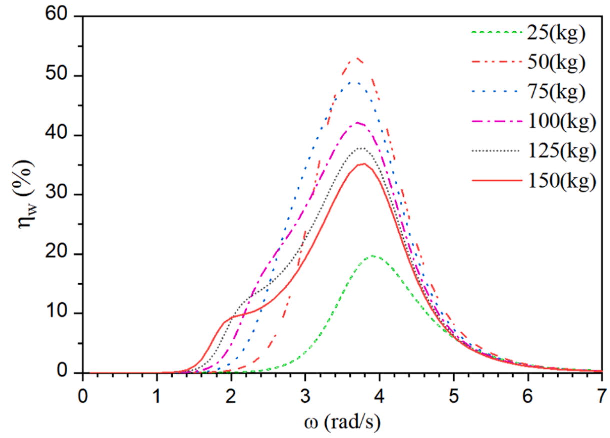

(c). Efficiency

Fig. 9. Response characteristics of the integrated system for varying m and ω.

parameters using the boundary element method. It also serves as a reference for selecting parameters in the subsequent physical model of IDWEC.

3.1. Hydrodynamic parameters and buoy model

Fig. 3(b) shows one of the most common types of marine buoys. This paper takes the 2.5 m diameter marine buoy as an example to study the coupled response characteristics of the buoy-IDWEC integrated system. Fig. 5 presents the model of the 2.5 m diameter marine buoy, along with the layout of the IDWEC within the integrated system. A Cartesian coordinate system O-xyz is set up with the center of the buoy's waterplane area as the origin, and the buoy's center of gravity is located directly below this origin. Since the total mass of the buoy and the IDWEC is constant, the buoy's displaced water volume and its hydrodynamic parameters remain unchanged.

A marine buoy with a diameter of 2.5 m was modeled using AQWA software, as shown in Fig. 6(a). The hydrodynamic parameters of the buoy for heave and pitch motions are presented in Figs. 6(b)–(f). According to the mathematical model in Section 2.2, the coupled motion response of the IDWEC-buoy integrated system in waves can be obtained by substituting these hydrodynamic parameters into the model.

3.2. Coupling resonance frequency of the integrated system

Damping and external forces do not affect the system's resonant frequency. Therefore, when analyzing the coupled resonant frequencies of an integrated system, damping can be neglected. Thus, the equations of motion for the integrated system can be written as:

$$\begin{bmatrix} M-m+A_{33} & A_{35} & 0 \\ A_{53} & I_{t5}+A_{55} & 0 \\ 0 & 0 & m \end{bmatrix} \begin{bmatrix} \ddot{\xi}_3 \\ \ddot{\xi}_{i3} \\ \ddot{\theta}_5 \end{bmatrix} + \begin{bmatrix} C_{33}+k_{PTO} & rk_{PTO} & -k_{PTO} \\ rk_{PTO} & C_{55}+r^2k_{PTO} & -rk_{PTO} \\ -k_{PTO} & -k_{PTO}r & k_{PTO} \end{bmatrix} \begin{bmatrix} \xi_3 \\ \xi_{i3} \\ \theta_5 \end{bmatrix} = \begin{bmatrix} 0 \\ 0 \\ 0 \end{bmatrix} \tag{22}$$

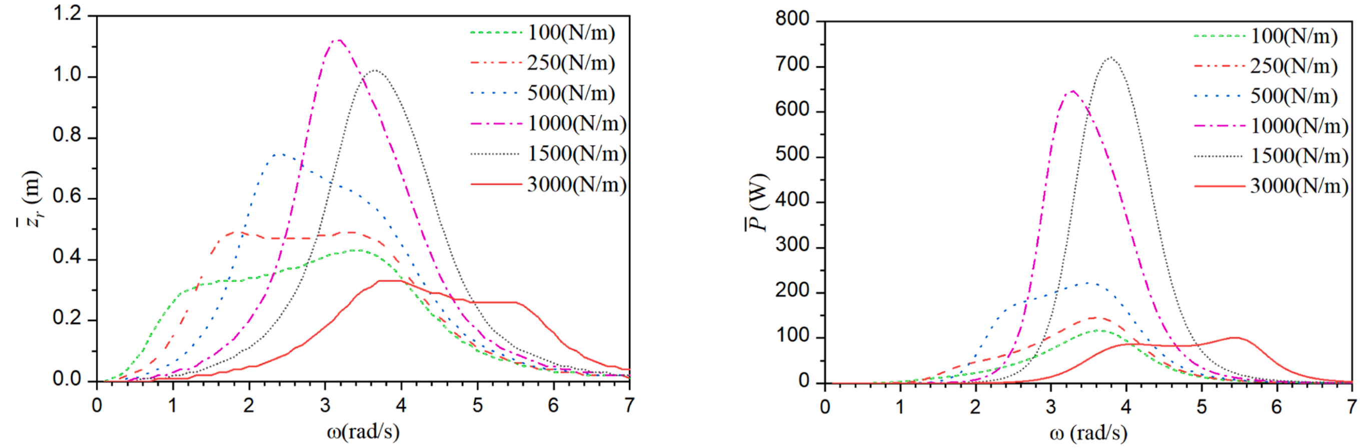

(a). Relative displacement (b). Average power

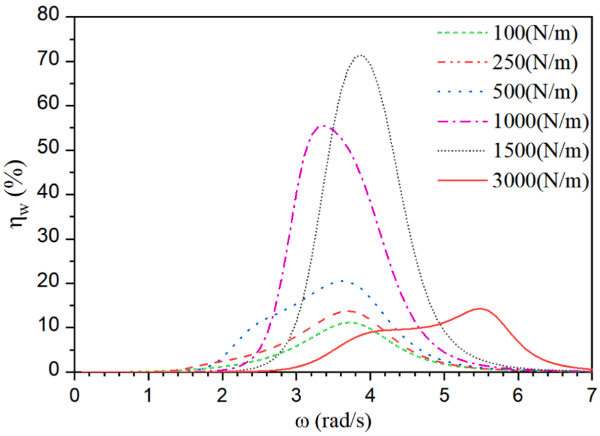

(c). Efficiency

Fig. 10. Response characteristics of the integrated system for varying k_{PTO} and ω.

Eq. (22) can also be expressed in the frequency domain as:

$$\begin{bmatrix} -\omega^2(M-m+A_{33})+(C_{33}+k_{PTO}) & -\omega^2A_{35}+rk_{PTO} & -k_{PTO} \\ -\omega^2A_{53}+rk_{PTO} & -\omega^2(I_{t5}+A_{55})+C_{55}+r^2k_{PTO} & -rk_{PTO} \\ -k_{PTO} & -k_{PTO}r & -\omega^2m+k_{PTO} \end{bmatrix} \begin{bmatrix} \xi_3 \\ \xi_{i3} \\ \theta_5 \end{bmatrix} = \begin{bmatrix} 0 \\ 0 \\ 0 \end{bmatrix} \tag{23}$$

The resonance frequency satisfies:

$$\det \begin{bmatrix} -\omega^2(M-m+A_{33})+(C_{33}+k_{PTO}) & -\omega^2A_{35}+rk_{PTO} & -k_{PTO} \\ -\omega^2A_{53}+rk_{PTO} & -\omega^2(I_{t5}+A_{55})+C_{55}+r^2k_{PTO} & -rk_{PTO} \\ -k_{PTO} & -k_{PTO}r & -\omega^2m+k_{PTO} \end{bmatrix} = 0 \tag{24}$$

By expanding the determinant, a cubic characteristic equation in terms of ω^2 can be obtained.

$$a(\omega^2)^3+b(\omega^2)^2+c(\omega^2)+d=0 \tag{25}$$

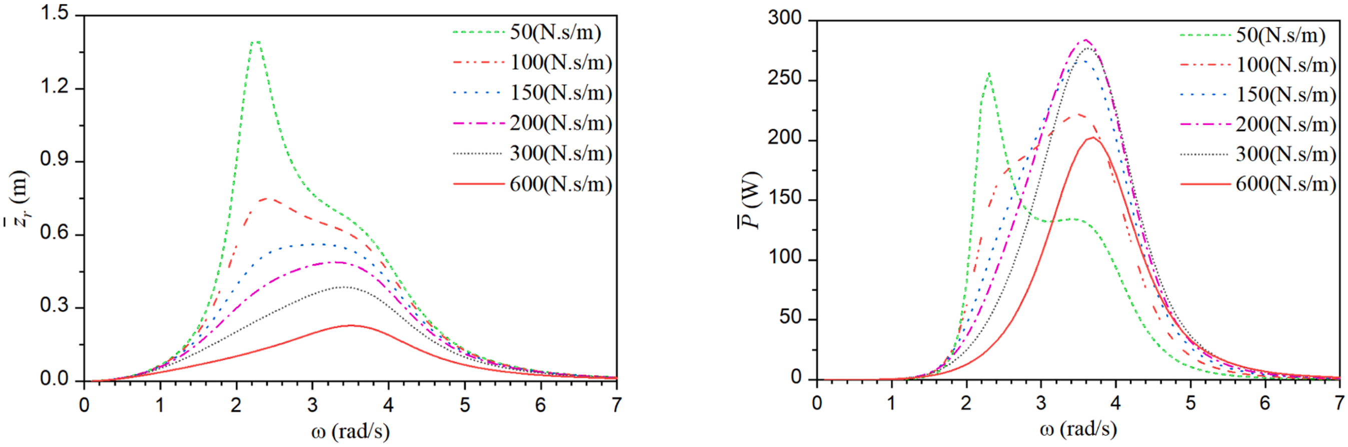

(a). Relative displacement　　(b). Average power

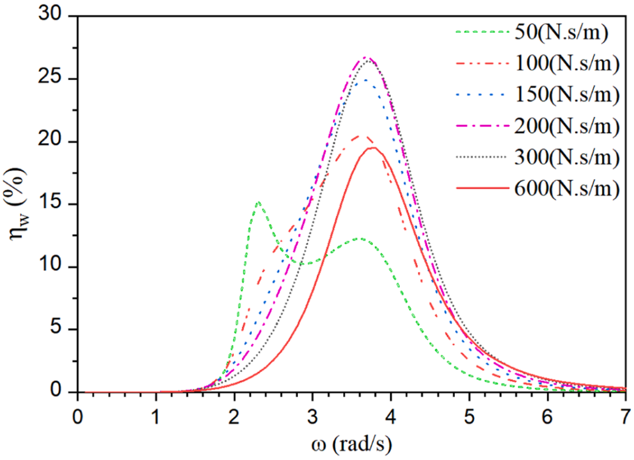

(c). Efficiency

Fig. 11. Response characteristics of the integrated system for varying C_{PTO} and ω.

where,

$$a = m\left[A_{35}A_{53} - (M - m + A_{33})(I_{t5} + A_{55})\right]$$

$$\begin{aligned} b = {} & m(C_{33} + k_{PTO})(I_{t5} + A_{55}) \\ & + (M - m + A_{33})\left[\left(C_{55} + r^2 k_{PTO}\right)m + k_{PTO}(I_{t5} + A_{55})\right] \\ & - mrk_{PTO}(A_{35} + A_{53}) - k_{PTO}A_{35}A_{53} \end{aligned}$$

$$\begin{aligned} c = {} & k_{PTO}C_{55}(M - m + A_{33}) - m(C_{33} + k_{PTO})\left(C_{55} + k_{PTO}r^2\right) \\ & - k_{PTO}(C_{33} + k_{PTO})(I_{t5} + A_{55}) + k_{PTO}^2\left(mr^2 + I_{t5} + A_{55}\right) \end{aligned}$$

$d = C_{55}C_{33}k_{PTO}$.

Fig. 7 presents cloud plots of the resonant frequencies of the integrated system as functions of varying m and k_{PTO} when $r = 1$ m. In Fig. 7 (a), the first resonant frequency ω_1 decreases with increasing m but increases with increasing k_{PTO}. ω_1 exhibits significantly higher sensitivity to variations in both m and k_{PTO}. In Fig. 7(b), the second resonant frequency ω_2 similarly decreases with increasing m and increases with increasing k_{PTO}. However, ω_2 shows significantly lower sensitivity to variations in m and k_{PTO}, and remains approximately at 3.7 rad/s – close to the pitch resonance frequency of the buoy. This indicates that ω_2 depends primarily on the inherent pitch characteristics of the buoy itself. In Fig. 7(c), the third resonant frequency ω_3 also shows relatively low sensitivity to variations in m and k_{PTO}, remaining approximately at 4 rad/s.

Fig. 8 illustrates the resonant frequencies of the integrated system under varying m or k_{PTO}. In Fig. 8(a), with $k_{PTO} = 500$N/m and $r = 1$m held constant, ω_1, ω_2, and ω_3 all decrease as m increases. In Fig. 8(b), with $m = 100$ kg and $r = 1$m held constant, ω_1, ω_2, and ω_3 all increases as k_{PTO} increases. When m increases, the frequency gap between the ω_1 and ω_3 first narrows and then widens; when k_{PTO}increases, this gap continuously narrows. These results indicate that for this integrated system, by setting appropriate values of m and k_{PTO}, the resonant frequency range of the integrated system can be broadened, thereby enhancing the power generation capacity of the IDWEC under different wave conditions.

3.3. Effect of ω and m

Fig. 9 illustrates the response characteristics of the integrated system for varying m and ω, with $k_{PTO} = 500$ N/m, $C_{PTO} = 100$ N.s/m, $r = 1$ m, and wave amplitude A = 0.25 m. In Fig. 9(a), as m increases, the relative displacement $\bar{z}_r$ curve gradually shifts from a single-peak shape to a double-peak shape. Furthermore, the effective frequency bandwidth between the two peaks gradually increases. In Fig. 9(b), as m increases, the average power P_{ave} curve also transitions from a single-peak to a double-peak shape. However, the maximum P_{ave} first increases and then decreases with increasing m. This indicates that a larger m is not necessarily better; it needs to be appropriately matched with k_{PTO} to

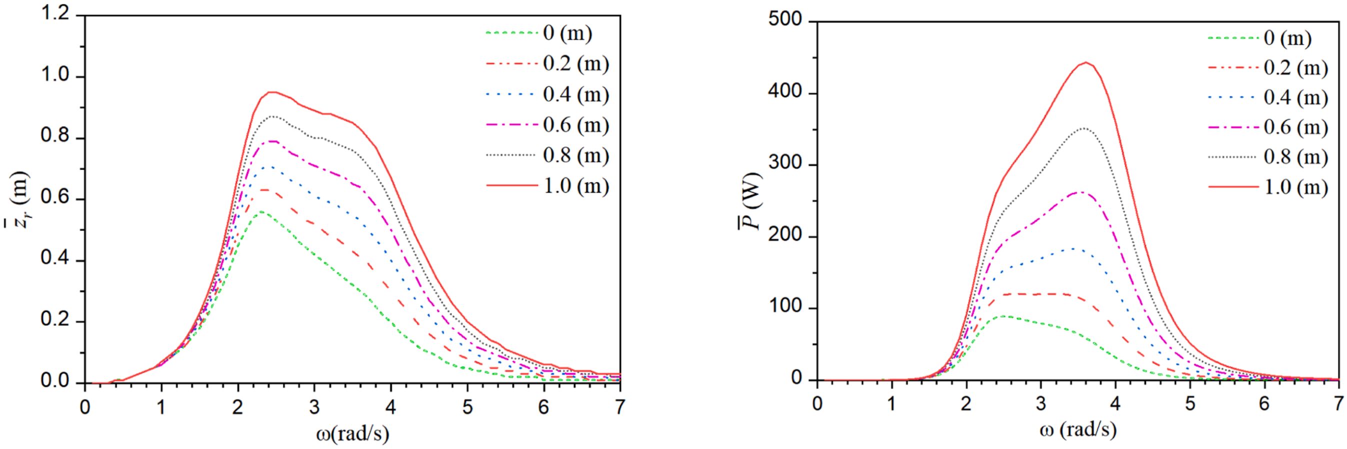

(a). Relative displacement

(b). Average power

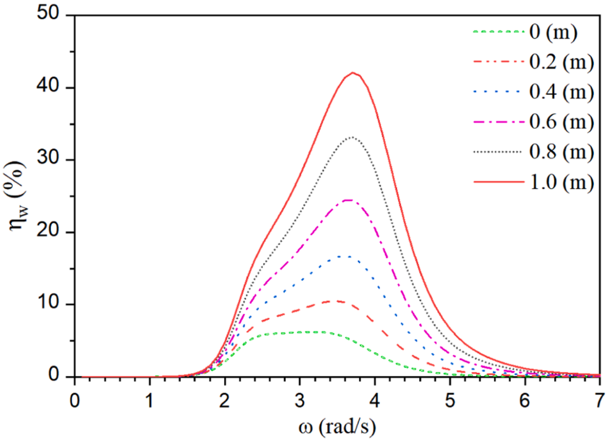

(c). Efficiency

Fig. 12. Response characteristics of the integrated system for varying r and ω.

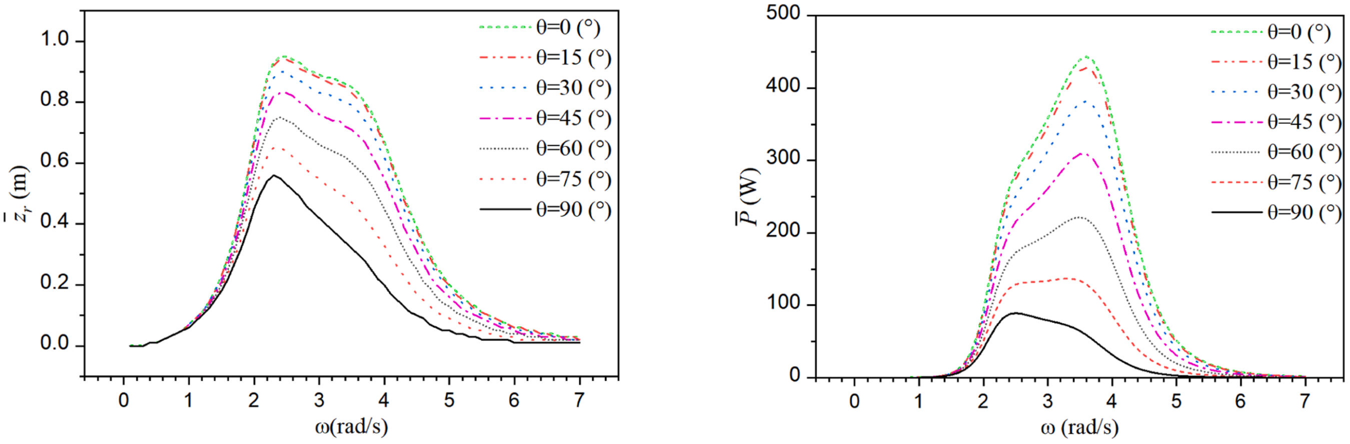

(a). Relative displacement

(b). Average power

Fig. 13. Response characteristics of the integrated system for varying θ and ω.

achieve better power generation. In Fig. 9(c), the double-peak characteristic of the power generation efficiency η_w curve becomes less pronounced as m increases. The maximum η_w also first increases and then decreases with increasing m, exceeding 50%. It can be observed from Fig. 9 that the response characteristics of the integrated system are significantly affected by both the natural pitch frequency of the buoy and the natural frequency of the spring-mass-damper system inside the IDWEC.

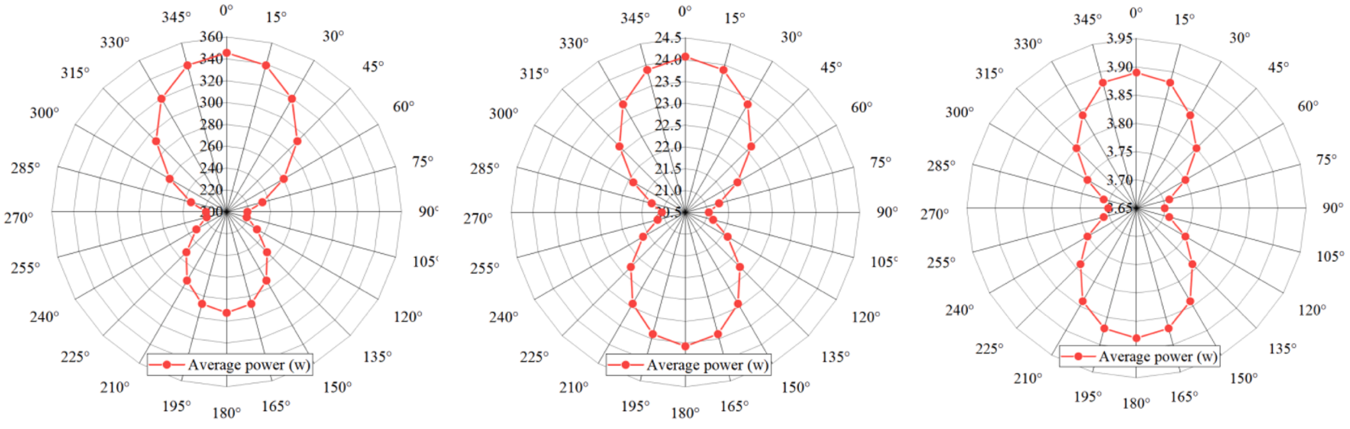

(a). T = 3 s, A = 0.5 m (b). T = 4 s, A = 0.5 m (c). T = 5 s, A = 0.5 m

Fig. 14. Average power of the integrated system for varying θ.

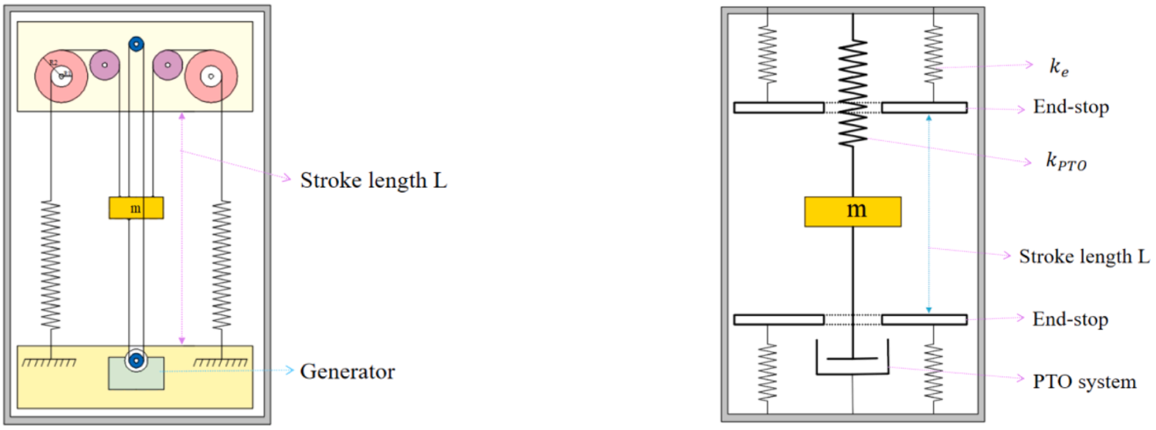

(a). Internal structure (b). Schematic diagram of internal structure

Fig. 15. Structural schematic diagram of IDWEC.

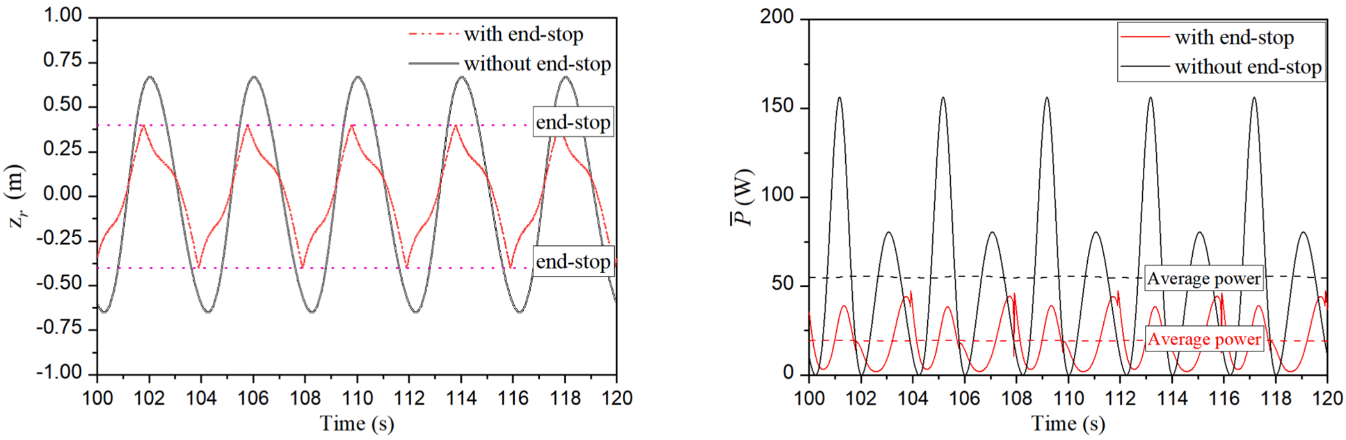

(a). Relative displacement (b). Instantaneous power and average power

Fig. 16. Response characteristics of the integrated system with and without an end-stop.

3.4. Effect of ω and k_{PTO}

Fig. 10 illustrates the response characteristics of the integrated system for varying k_{PTO} and ω, with m =100 kg, C_{PTO} =100 N.s/m, $r = 0.5$ m, and wave amplitude $A = 0.25$ m. In Fig. 10(a), as the spring stiffness k_{PTO} increases, the relative displacement $\overline{z}_r$ curve gradually shifts from a dual-peak shape to a single peak and then back to a dual-peak shape. The maximum $\overline{z}_r$ value first increases and then decreases. $\overline{z}_r$ reaches its

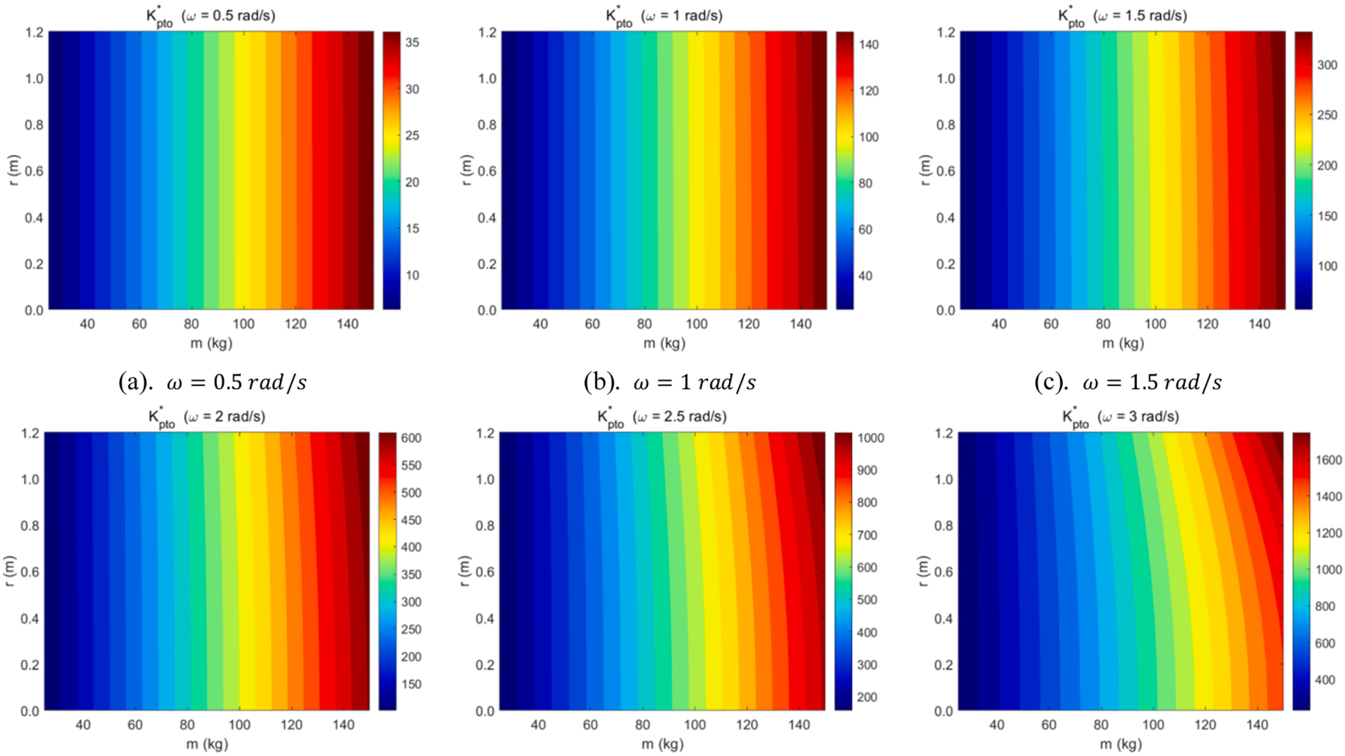

(a). $\omega = 0.5\ rad/s$ (b). $\omega = 1\ rad/s$ (c). $\omega = 1.5\ rad/s$

(d). $\omega = 2\ rad/s$ (e). $\omega = 2.5\ rad/s$ (f). $\omega = 3\ rad/s$

Fig. 17. The optimal spring stiffness k^*_{PTO} for varying m and r.

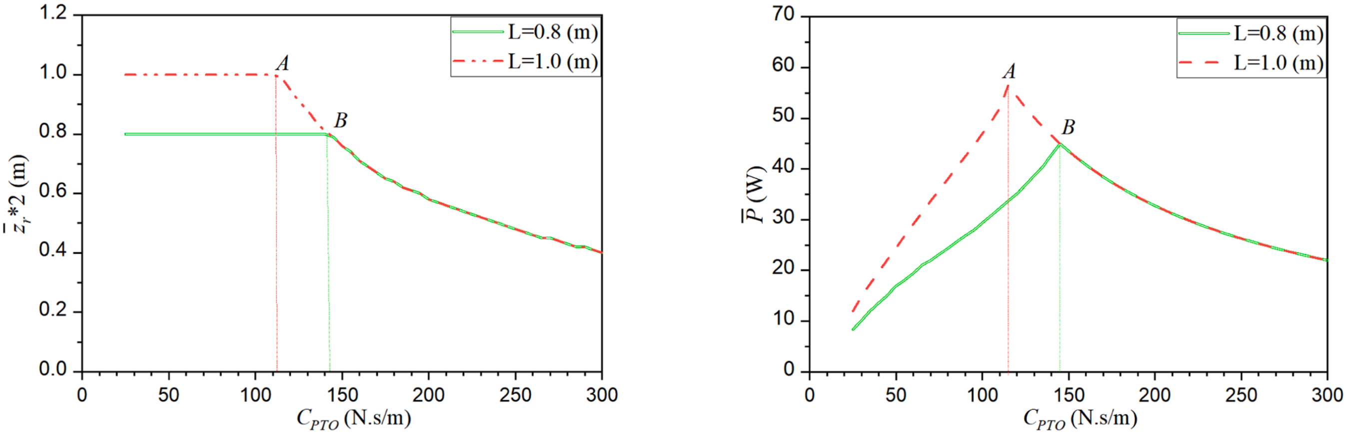

(a). Relative displacement (b). Average power

Fig. 18. Nonlinear response characteristics of the integrated system for varying L and C_{PTO}.

maximum when the natural frequency of the spring-mass-damper system inside the IDWEC approaches the natural pitch frequency of the buoy. In Fig. 10(b), the average power P_{ave} curve similarly transitions from a dual-peak shape to a single peak and then back to a dual-peak shape as k_{PTO} increases. The maximum P_{ave} first increases and then decreases with increasing k_{PTO}. When k_{PTO} is either large or small, the emergence of dual-resonance frequencies enhances the IWEC's adaptability to different wave conditions. However, the maximum average power exhibits a significant reduction compared to that at the single-peak resonance frequency. In Fig. 10(c), the power generation efficiency η_w exhibits the same response characteristics as the average power P_{ave}, with a maximum efficiency exceeding 70%.

3.5. Effect of ω and C_{PTO}

Fig. 11 illustrates the response characteristics of the integrated system for varying C_{PTO} and ω, with $m = 100$ kg, $k_{PTO} = 500$ N/m, $r = 0.5$ m, and wave amplitude $A = 0.25$ m. In Fig. 11(a), as the damping coefficient C_{PTO} increases, the relative displacement $\bar{z}_r$ curve gradually transitions from a dual-peak shape to a single-peak shape, and the maximum $\bar{z}_r$ value decreases progressively. When C_{PTO} is small, the emergence of dual-resonance frequencies enhances the IWEC's adaptability to different wave conditions. However, the significant increase in the maximum $\bar{z}_r$ value increases the stroke length L required within the IWEC to accommodate the sliding body's motion. In Fig. 11(b), the average power Pve curve similarly transitions from a dual-peak shape to

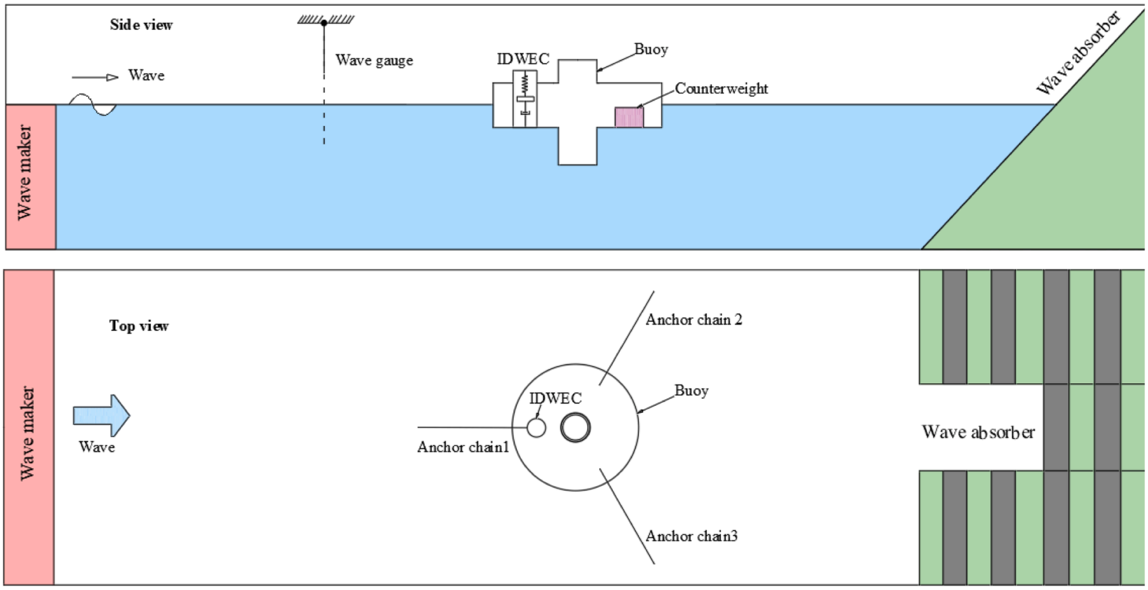

(a) Schematic diagram of wave tank testing experiment

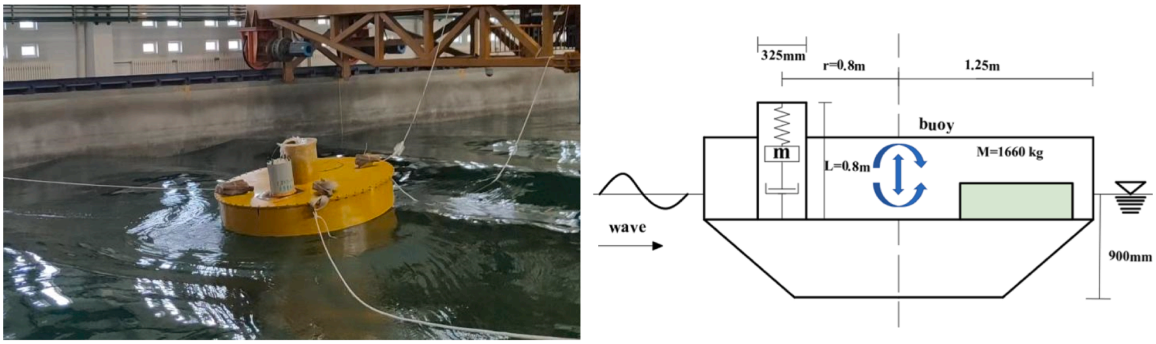

(b) Physical models of the IDWEC and buoy

(c) Main parameters of IDWEC and buoy

Fig. 19. Wave tank testing experiment.

a single-peak shape as cPTO increases. The maximum P_{ave} first increases and then decreases with increasing C_{PTO}. In Fig. 11(c), the power generation efficiency η_w exhibits response characteristics identical to the average power, with a maximum efficiency exceeding 25%.

3.6. *Effect of ω and r*

Fig. 12 illustrates the response characteristics of the integrated system for varying r and ω, with $m = 100$ kg, $k_{PTO} = 500$ N/m, $C_{PTO} = 100$ N.s/m, and wave amplitude $A = 0.25$ m. In Fig. 12(a), as the lever arm r increases, the relative displacement $\bar{z}_r$ curve transitions from a single-peak shape to a double-peak shape. The frequency of the second peak corresponds to the buoy's natural pitch frequency, and the maximum $\bar{z}_r$ increases monotonically. In Fig. 12(b), the average power

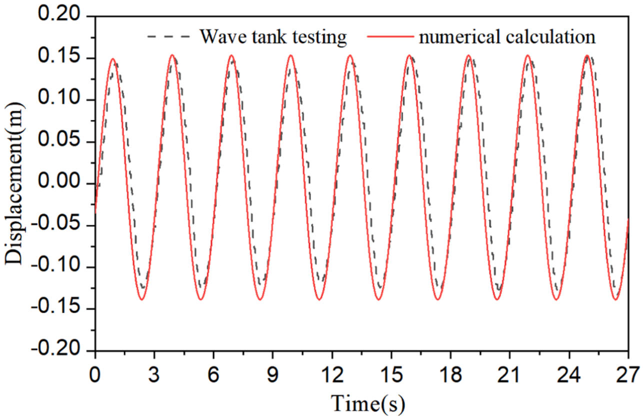

Fig. 20. Comparison of the relative displacements between wave tank testing and numerical calculation.

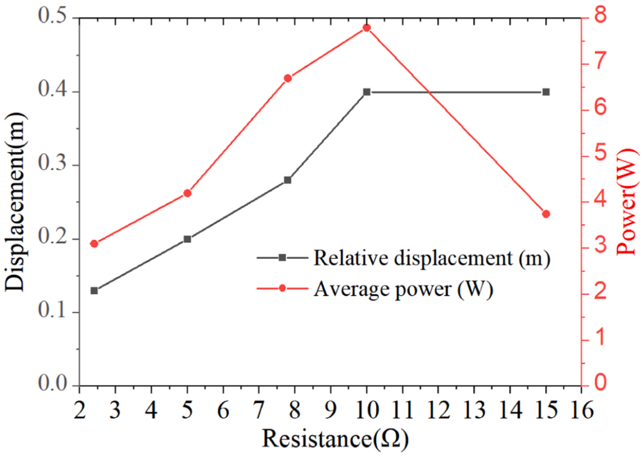

Fig. 21. Influence of different resistances on the motion response and power generation performance of the IDWEC.

P_{ave} curve similarly shifts from a single peak to a double peak as the lever arm r increases, with the maximum P_{ave} also increasing with larger r. In Fig. 12(c), the power generation efficiency η_w exhibits the same response characteristics as the P_{ave}, with the maximum efficiency exceeding 40%. The above results demonstrate that increasing the lever arm r has a unidirectional and significant effect on improving the performance of the IDWEC.

3.7. Effect of ω and θ

Fig. 13 illustrates the response characteristics of the integrated system for varying θ and ω, with $m = 100$ kg, $k_{PTO} = 500$ N/m, $C_{PTO} = 100$ N.s/m, $r = 1$ m, and wave amplitude $A = 0.25$ m. In Fig. 13(a), as the wave incident angle θ increases, the relative displacement $\bar{z}_r$ curve gradually transitions from a double-peak shape to a single-peak shape, and the maximum $\bar{z}_r$ value gradually decreases. In Fig. 13(b), the average power P_{ave} curve similarly shifts from a double-peak to a single-peak shape as θ increases, and the maximum P_{ave} decreases with increasing θ. The above results indicate that the effect of the wave incident angle θ is equivalent to only changing the lever arm r. When the wave incident angle $\theta = 90^\circ$, r is 0 m.

Fig. 14 illustrates the average power of the integrated system for varying θ, with $m = 100$ kg, $k_{PTO} = 500$ N/m, $C_{PTO} = 100$ N·s/m, $r = 1$ m, and wave amplitude $A = 0.5$ m. In Fig. 14(a), for a wave period of T = 3 s, the average power P_{ave} reaches its maximum value of 345.5 W at $\theta = 0^\circ$ and its minimum value of 218.91 W at $\theta = 90^\circ$ Over the full range of θ from 0° to 360°, P_{ave} varies between 218.91 W and 345.5 W. Similarly, in Fig. 11(b) for T = 4 s, P_{ave} ranges from 21.04 W to 24.07 W. In Fig. 14(c) for T = 5 s, P_{ave} ranges from 3.70 W to 3.89 W. These results demonstrate that the wave period significantly impacts the IDWEC's performance. When arranging the position of the IDWEC, it should be oriented such that the wave incident direction should be as parallel as possible to the connection between the center of gravity of the IDWEC and the center of gravity of the buoy.

4. Nonlinear constraints between IDWEC and buoy

Fig. 15 illustrates the schematic structure diagram of the IDWEC. During actual operation, the motion of the sliding body is constrained by the internal structural space of the IDWEC, particularly in the vertical direction. The sliding body has a stroke length L. When the relative displacement of the sliding body exceeds $\pm L/2$, it collides with the upper and lower end-stops of the IDWEC, thereby reducing its kinetic energy. Eq. (26) gives the expression for the PTO force under both collision and non-collision conditions of the sliding body.

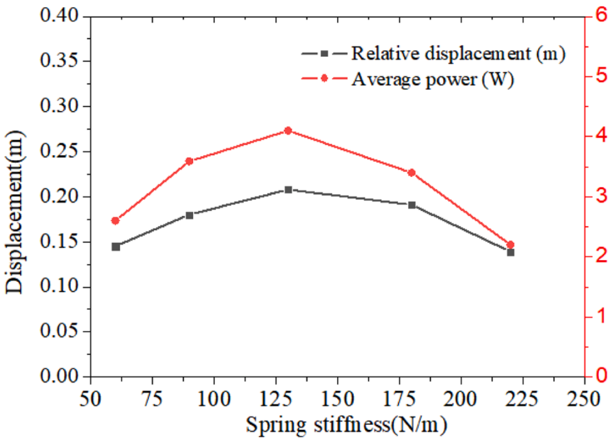

Fig. 22. Influence of different spring stiffness on the motion response and power generation performance of the IDWEC.

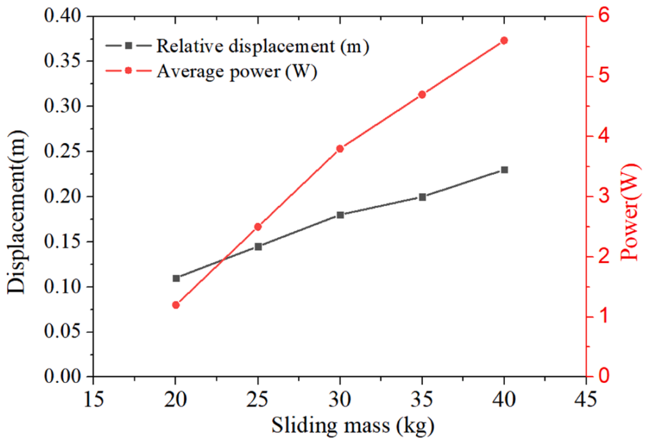

Fig. 23. Influence of different sliding bodyes on the motion response and power generation performance of the IDWEC.

$$F_{PTO} = \begin{cases} -C_{PTO}(\dot{\xi}_3 + r\dot{\theta}_5 - \dot{\xi}_{i3}) - k_{PTO}(\xi_3 + r\theta_5 - \xi_{i3}) & |\bar{z}_r| \leq L/2 \\ -C_{PTO}(\dot{\xi}_3 + r\dot{\theta}_5 - \dot{\xi}_{i3}) - (k_{PTO} + k_e)(\xi_3 + r\theta_5 - \xi_{i3}) & |\bar{z}_r| > L/2 \end{cases} \tag{26}$$

where, k_e is the spring stiffness of the end-stop, which can be considered infinite.

Fig. 16 shows the relative displacement and power of the integrated system with and without an end-stop under the conditions of wave period $T = 4$ s, wave amplitude $A = 0.75$ m, $m = 100$ kg, $k_{PTO} = 500$ N/m, $C_{PTO} = 100$ N.s/m, $r = 1$ m, and stroke length $L = 0.8$ m. In Fig. 16(a), for the integrated system without end-stops, the maximum relative displacement $\bar{z}_r$ is 0.72 m. In contrast, for the integrated system with end-stops, the maximum $\bar{z}_r$ is 0.4 m. For the system with end-stops, when $\bar{z}_r$ exceeds $L/2$, it collides with the end-stop and rebounds immediately. Furthermore, Fig. 16(b) shows that collision with the end-stop results in a reduction in instantaneous power. Consequently, the overall average power of the integrated system with end-stops is significantly lower than that of the integrated system without end-stops.

4.1. The optimal spring stiffness of the integrated system

According to Eq. (24), for a given wave frequency ω, if det(Z) = 0, the integrated system resonates. At this time, the output power of the system reaches its maximum. Thus, the expression for the optimal spring stiffness coefficient k^*_{PTO} can be derived as follows:

$$k^*_{PTO} = \frac{\omega^2 m\{[-\omega^2(M-m+A_{33})+C_{33}][-\omega^2(I_{55}+A_{55})+C_{55}]-(\omega^4 A_{35}^2)\}}{[-\omega^2(M-m+A_{33})+C_{33}][-\omega^2(I_{55}+A_{55})+C_{55}]-(\omega^4 A_{35}^2)+\omega^2 m\{2(-\omega^2 A_{35})r-[-\omega^2(M-m+A_{33})+C_{33}]r^2-[-\omega^2(I_{55}+A_{55})+C_{55}]\}} \tag{27}$$

Fig. 17 shows the optimal spring stiffness k^*_{PTO} of the integrated system for varying m and r at a given wave frequency ω. From Figs. 17(a) to (f), it can be observed that the mass m exerts a significant influence on k^*_{PTO}. When m is small, the effect of the lever arm r on k^*_{PTO} is minimal and almost negligible. However, as m increases, the influence of r on k^*_{PTO} becomes increasingly pronounced. For a spring-mass-damper system, the resonant spring stiffness can be expressed as $\omega^2 m$. Consequently, when m is small, k^*_{PTO} closely approximates this formula.

4.2. The nonlinear response characteristics of the integrated system

Fig. 18 illustrates the nonlinear response characteristics of the integrated system for varying L and C_{PTO}, with $m = 100$ kg, $k_{PTO} = k^*_{PTO}$, $r = 1$ m, wave amplitude $A = 0.25$ m, and a given wave frequency $\omega = 2$ rad/s. In Fig. 18(a), for both stroke lengths $L = 0.8$ m and $L = 1.0$ m, the

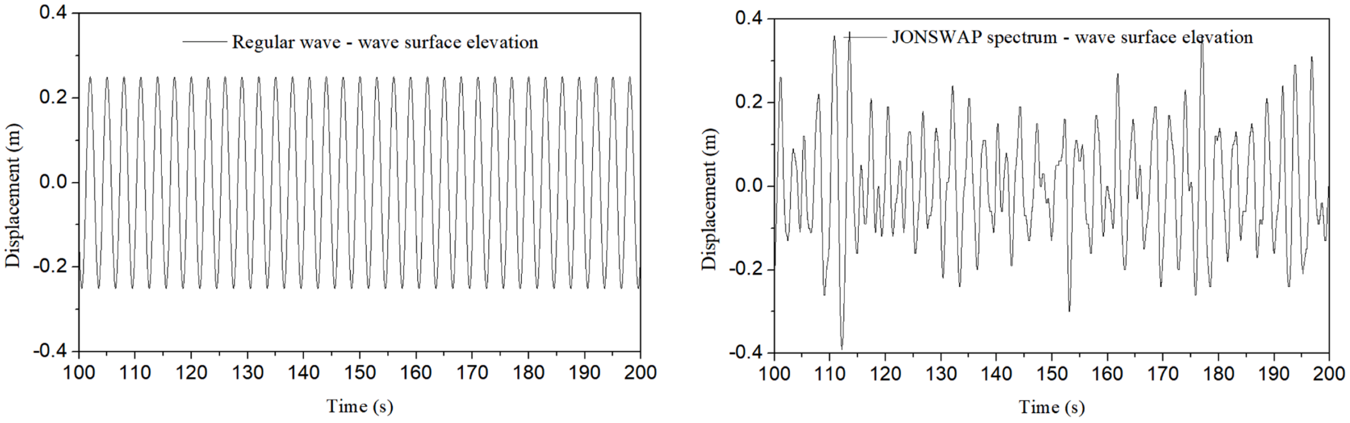

(a). Regular wave

(b). Irregular wave

Fig. 24. Wave surface elevation under JONSWAP spectrum and regular waves.

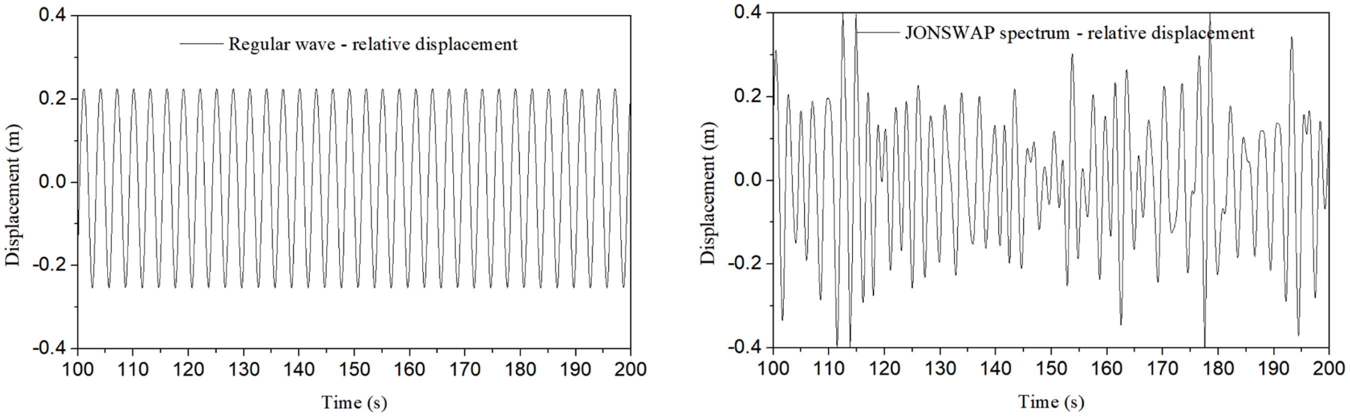

(a). Regular wave

(b). Irregular wave

Fig. 25. Relative displacement under JONSWAP spectrum and regular waves.

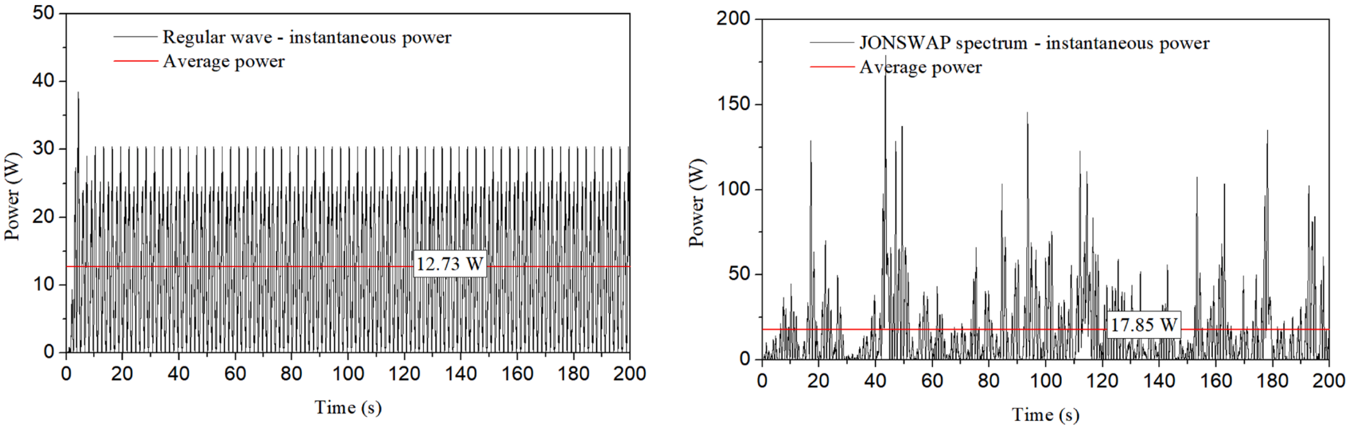

(a). Regular wave

(b). Irregular wave

Fig. 26. Instantaneous and average power of the IDWEC under JONSWAP spectrum and regular waves.

relative displacement amplitude $\bar{z}_r$ initially remains constant and then gradually decreases as C_{PTO} increases. This constant region is caused by the end-stop restricting the motion of the sliding body. The C_{PTO} values corresponding to points A and B are 115 N.s/m and 145 N.s/m, respectively. In Fig. 18(b), the average power P_{ave} first increases and then decreases with increasing C_{PTO}. For stroke lengths $L = 0.8$ m and $L = 1.0$ m, the maximum P_{ave} values are 45 W and 52 W, respectively, achieved at corresponding C_{PTO} values of 145 N.s/m and 115 N.s/m. From these results, it can be observed that for a given wave frequency ω and stroke length L, the optimal C_{PTO} occurs when $\bar{z}_r$ reaches $L/2$.

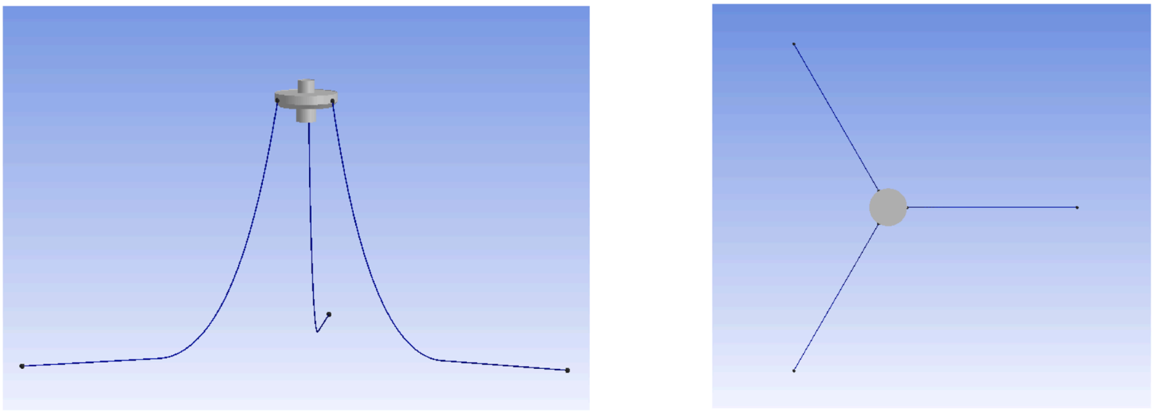

(a). Side view

(b). Top view

Fig. 27. Schematic diagram of a full-size test model.

Table 2
Main parameters of the full-scale testing model.

Buoy		IDWEC		Mooring System	
Parameter	Value	Parameter	Value	Parameter	Value
Diameter of buoy	2.5 m	Mass of sliding body	40 kg	Number of anchor chains	3
Mass of buoy	1660 kg	Stroke length	0.8 m	Length of anchor chain	45 m
Draft of buoy	0.9 m	Spring stiffness	300 N/m	Diameter of anchor chain	50 mm
Lever arm	0.8 m	PTO damping	75 N. s/m	Break load of anchor chain	2660,000 N

5. Model experiment in wave tank

This section describes the physical model of the IDWEC integrated with a buoy and presents regular/random wave testing conducted on the integrated system in a wave tank. First, the consistency between numerical simulation data and wave-tank experimental data was validated. Then, the effects of the sliding body, spring stiffness, and external electrical load on the IDWEC's power generation performance were analyzed.

5.1. *Experimental setup and model*

Fig. 19 shows the schematic diagram and physical model of the wave-tank experiment, including the main parameters of the IDWEC and

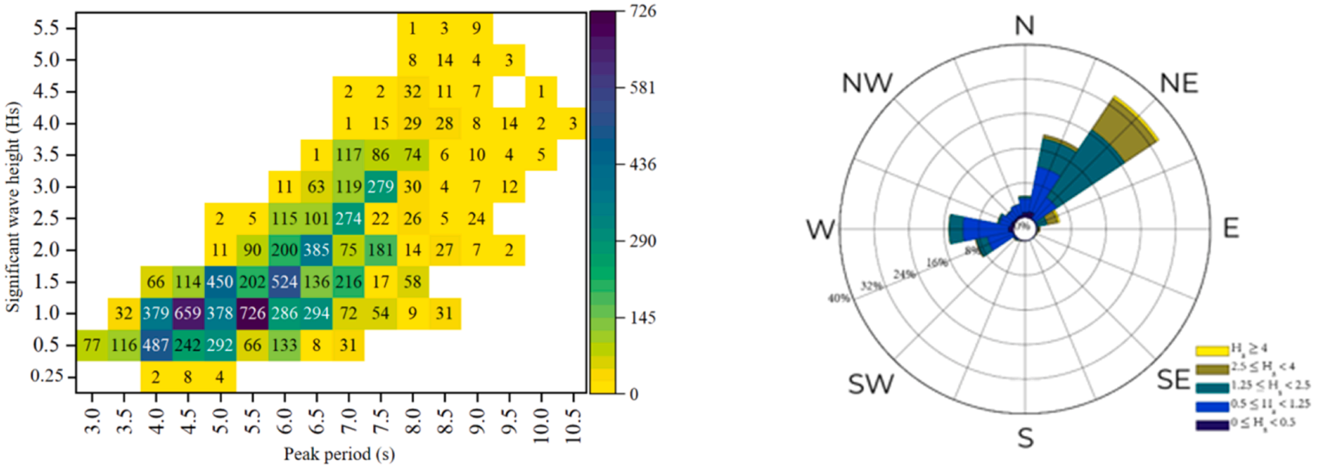

(a) wave scatter diagram of the South China Sea in 2022

(b) Rose chart of significant wave height and wave direction

Fig. 28. Distribution of wave conditions in the South China Sea in 2022.

Table 3
The maximum tension load of anchor chains under several extreme wave conditions.

Wave conditions	Anchor Chain Number			Wave conditions	Anchor Chain Number		
	1 (N)	2 (N)	3 (N)		1 (N)	2 (N)	3 (N)
$T_p = 7\ s,\ H_s = 4.5\ m$	116,280	8925	9271	$T_p = 9\ s,\ H_s = 5.5\ m$	141,942	16,463	18,073
$T_p = 7.5\ s,\ H_s = 4.5\ m$	83,001	18,574	6563	$T_p = 9.5\ s,\ H_s = 5\ m$	31,898	7636	2934
$T_p = 8\ s,\ H_s = 5.5\ m$	114,391	6970	13,793	$T_p = 10\ s,\ H_s = 4.5\ m$	25,720	2686	2503
$T_p = 8.5\ s,\ H_s = 5.5\ m$	86,508	8508	8766	$T_p = 10.5\ s,\ H_s = 4\ m$	10,580	1587	2191

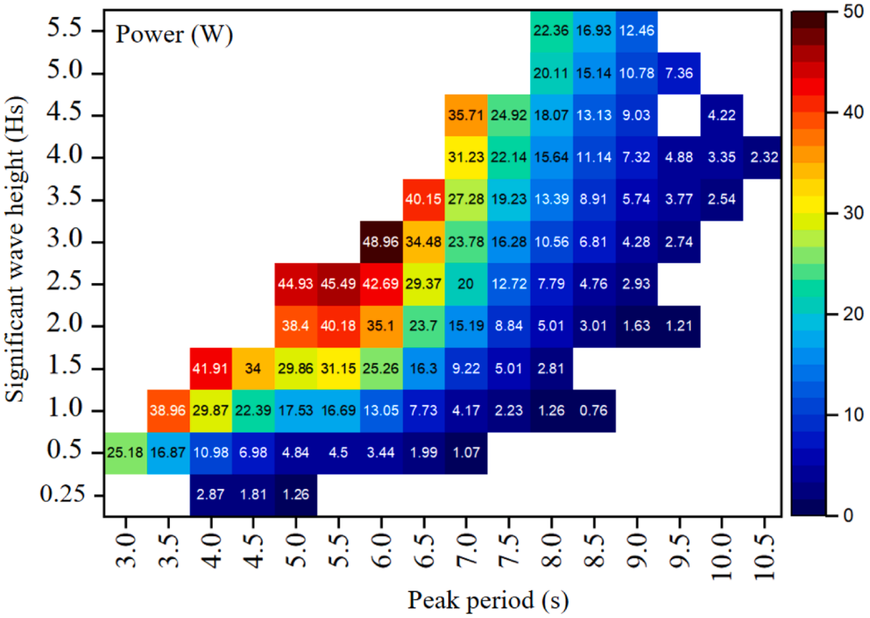

Hs \ Peak period (s)	3.0	3.5	4.0	4.5	5.0	5.5	6.0	6.5	7.0	7.5	8.0	8.5	9.0	9.5	10.0	10.5
5.5											22.36	16.93	12.46			
5.0											20.11	15.14	10.78	7.36		
4.5									35.71	24.92	18.07	13.13	9.03		4.22	
4.0									31.23	22.14	15.64	11.14	7.32	4.88	3.35	2.32
3.5								40.15	27.28	19.23	13.39	8.91	5.74	3.77	2.54	
3.0							48.96	34.48	23.78	16.28	10.56	6.81	4.28	2.74		
2.5					44.93	45.49	42.69	29.37	20	12.72	7.79	4.76	2.93			
2.0					38.4	40.18	35.1	23.7	15.19	8.84	5.01	3.01	1.63	1.21		
1.5			41.91	34	29.86	31.15	25.26	16.3	9.22	5.01	2.81					
1.0		38.96	29.87	22.39	17.53	16.69	13.05	7.73	4.17	2.23	1.26	0.76				
0.5	25.18	16.87	10.98	6.98	4.84	4.5	3.44	1.99	1.07							
0.25			2.87	1.81	1.26											

Fig. 29. Average power of the IDWEC under different random wave conditions.

the buoy. The wave tank is 130 m long, 18 m wide, and 6 m deep, and can simulate regular and random waves with wave heights ranging from 0 to 0.6 m. The main parameters of the buoy and IDWEC are shown in Fig. 19(c). The buoy was loosely moored near the center of the wave tank using three anchor chains positioned at 120-degree intervals. A wave gauge was installed 5 m in front of the buoy to record the time-history curve of the wave-surface elevation. A miniature displacement sensor was installed inside the IDWEC to measure the relative displacement between the sliding body and the buoy. The alternating current (AC) generated by the IDWEC's generator was first rectified through a bridge rectifier before being converted into direct current (DC) to supply power to the external electrical load.

5.2. *Experimental results and analysis*

To verify the consistency of the numerical calculation results, a comparison was conducted between the numerical calculations and the wave tank testing results. Fig. 20 presents the comparison of the relative displacement of the sliding body between the wave tank testing and numerical calculation under regular wave conditions with a 3 s wave period and 0.25 m wave height, while maintaining identical parameters. The comparison revealed that the numerical calculations exhibited good agreement with the wave tank testing results, thereby validating the reliability of the established mathematical model.

The external electrical load of the IDWEC employs a sliding rheostat with adjustable resistance. Fig. 21 shows the influence of different resistances on the motion response and power generation performance of the IDWEC under test conditions of regular waves with a period of 3 s, wave height of 0.25 m, m =30 kg, and k_{PTO} =132 N/m. The relative displacement $\overline{z}_r$ initially increases gradually with increasing resistance and then stabilizes. The main reason is that higher resistance leads to smaller current in the circuit, resulting in reduced impedance from the PTO system, thereby enhancing the motion of the sliding body. However, since the motion of the IDWEC is constrained by its finite stroke length L, the relative displacement $\overline{z}_r$ remains constant at higher resistance values. As the resistance value increases, the average power P_{ave} of the IDWEC initially increases and then decreases. The maximum P_{ave} is achieved when the maximum $\overline{z}_r$ reaches half the IDWEC's stroke length ($L/2$). This result is consistent with the findings shown in Fig. 18, validating the response characteristics of the integrated system described above.

Fig. 22 shows the influence of different spring stiffness values on the motion response and power generation performance of the IDWEC under test conditions, which included regular waves with a period of 3 s, a wave height of 0.25 m, m = 30 kg, and a 5 Ω load resistance. Both the relative displacement $\overline{z}_r$ and average power P_{ave} initially increase with spring stiffness P_{ave} but then decrease upon further increase. The maximum $\overline{z}$ and P_{ave} occur when the resonance frequency of the IDWEC's internal spring-mass-damping system approaches the wave frequency. These results indicate that when selecting spring stiffness, the natural frequency of the spring-mass system should be tuned as close as possible to the most probable wave frequency in real sea states.

Fig. 23 shows the influence of the sliding body mass on the motion response and power generation performance of the IDWEC under test conditions of regular waves with a period of 3 s, wave height of 0.25 m, k_{PTO} =132 N/m, and a 5 Ω load resistance. Both the relative displacement and average power exhibited proportional increases with sliding body mass, showing linear growth trends. The above results indicate that the mass of the sliding body should be increased as much as possible, within the constraints of the IDWEC's allowable internal space, to enhance the output power.

6. Coupling response characteristics of the integrated system under real sea wave conditions

This section analyzes the motion response and energy conversion characteristics of the IDWEC under the JONSWAP wave spectrum. The average daily power generation of the IDWEC is predicted based on the 2022 wave scatter diagram for the South China Sea area.

6.1. *Motion response and power generation performance of the IDWEC under JONSWAP spectrum*

Fig. 24 compares the wave surface elevation under the JONSWAP spectrum with that of regular waves. The JONSWAP spectrum was characterized by a significant wave height of 0.5 m and a peak wave period of 3 s, while the regular waves had a wave height of 0.5 m and a wave period of 3 s.

Fig. 25 shows the relative displacement of the sliding body under both JONSWAP spectrum and regular waves, with test conditions of L = 0.8 m, k_{PTO} = 132 N/m, m = 40 kg, and C_{PTO} = 100 N·s/m. Under regular waves, the relative displacement exhibits sinusoidal characteristics, whereas under the JONSWAP spectrum, it demonstrates randomness.

Fig. 26 presents the instantaneous power and average power of the IDWEC under both the JONSWAP spectrum and regular waves. Under the JONSWAP spectrum, the IDWEC achieved a maximum instantaneous power of 175 W and an average power of 17.85 W. In regular waves, the maximum instantaneous power was 30 W, with an average power output of 12.73 W. The results indicate that the IDWEC also demonstrates reliable power generation capability under the JONSWAP spectrum, with slightly higher power generation performance than that in regular waves under this condition. This is primarily attributed to the more frequent oscillations of the sliding body under the JONSWAP spectrum.

6.2. *Daily average power generation forecast of the integrated system*

To analyze the power generation capability of the integrated system under real sea states, a full-scale test model (shown in Fig. 27) was developed. The test model comprises a buoy, an IDWEC, and a mooring system. The parameters of the full-scale test model are detailed in Table 2.

The water depth is 30 m, and the random wave conditions in this sea area conform to the standard JONSWAP spectrum model described in Section 2.2. The mooring system consists of three anchor chains, each 45 m in length, with a breaking load of 2660,000 N.

Fig. 28 presents the distribution of wave conditions in the South China Sea for 2022. Fig. 28(a) shows the wave scatter diagram for that year. Each cell records the total hours the corresponding wave condition occurred (e.g., the value 77 at T_p =3 s, H_s =0.5 m indicates this condition lasted 77 h throughout 2022). The diagram reveals that wave periods are primarily concentrated between 3–8 s, while significant wave heights are mainly distributed from 0.5 m to 3.5 m. Fig. 28(b) displays the wave rose diagram for significant wave height and wave direction, showing relatively concentrated wave directions, predominantly from the NE (Northeast). Given this concentration, this study assumes all waves originate from the NE direction when calculating the IDWEC's daily average power generation prediction, setting NE as the 0° wave direction.

The daily average power generation of IDWEC can be obtained through the following equation:

$$\overline{P}_D = \frac{\sum_{i=3}^{10.5}\sum_{j=0.25}^{5.5} H_{ij}\overline{P}_{ij}}{\sum_{i=3}^{10.5}\sum_{j=0.25}^{5.5} H_{ij}} * 24 \tag{28}$$

where, i represents the peak period, j represents the significant wave height, $\overline{P}_{ij}$ represents the average power of the IDWEC under peak period i and significant wave height j, and H_{ij} represents the number of hours corresponding to peak period i and significant wave height j.

Table 3 presents the maximum tension forces experienced by different anchor chains under several extreme wave conditions depicted in Fig. 28(a). The maximum tension force on an anchor chain occurs under the wave condition of $T_p = 9$ s and $H_s = 5.5$ m, specifically on Anchor Chain 1, reaching 141,942 N. This value is less than the anchor chain's breaking load of 2660,000 N. Therefore, the buoy can operate safely under the wave conditions shown in Fig. 28(a).

Fig. 29 presents the average power generation forecast of the IDWEC under different wave conditions modeled using the JONSWAP spectrum. The wave conditions correspond to those in Fig. 28(a). Except for the tested wave conditions, all other parameters remained unchanged: the wave direction was fixed at 0°, the stroke length $L = 0.8$ m, the PTO damping was set to 75 N.s/m, and the spring stiffness was maintained at 300 N/m. As the peak period increased, the IDWEC's average power gradually decreased, while larger significant wave heights led to a progressive increase in its average power. By combining the results from Fig. 28(a) and Fig. 29 and utilizing Eq. (28), the daily average power generation of the IDWEC under random wave conditions in the South China Sea in 2022 was forecast to be 455.92 Wh. According to the research by Wang et al. (2022) and Chen et al. (2025), the hydro-meteorological sensors installed on the buoy collect and transmit data every 10 min, requiring a daily energy consumption of 395.92 Wh. Therefore, the IDWEC designed in this study, with parameters $C_{PTO} = 75$ N.s/m, $k_{PTO} = 300$ N/m, $r = 0.8$ m, and $m = 40$ kg, is sufficient to meet the buoy's daily power requirements.

7. Conclusions

To address the frequent power shortages faced by marine buoys in deep-sea environments, this paper proposes a novel IDWEC. The IDWEC can be installed within a buoy to form an integrated system. As the IDWEC does not directly contact seawater, it exhibits enhanced reliability and survivability. To establish an effective wave energy capture mechanism, a mathematical model for the integrated system's energy conversion was developed using the Boundary Element Method. This paper investigates the influence of various factors on the motion response and energy conversion characteristics of the IDWEC, analyzes its performance differences under regular and irregular waves, and validates the numerical results through wave tank experiments. Based on the numerical simulations and experimental results, the following conclusions can be drawn:

1. The IDWEC-Buoy Integrated System features three distinct resonance frequencies. These resonance frequencies can be adjusted by changing the mass of the sliding body or the spring stiffness to match the wave conditions in the target sea area, thereby enhancing power output.
2. When the mass of the sliding body is small, the three resonance frequencies correspond respectively to the natural heave frequency of the buoy, the natural pitch frequency of the buoy, and the natural frequency of the internal spring-mass-damper system within the IDWEC. This latter natural frequency can be approximately $\omega^2 m$.
3. The optimal spring stiffness is independent of the PTO damping coefficient. However, for an IDWEC with limited internal volume, the optimal PTO damping—and thus the maximum power output—is achieved when the relative displacement amplitude of the sliding body under the optimal spring stiffness is precisely equal to half of the device's stroke length ($L/2$).
4. Based on the 2022 wave scatter diagram for the South China Sea area, the IDWEC system with m =40 kg, k_{PTO} =300 N/m, C_{PTO}=75 N/(m/s), L =0.8 m, and r =0.8 m achieves a daily average power generation of 455.92 Wh under random wave conditions. This output meets the daily average power demand of 395.92 Wh required by the sensors in 2.5 m diameter buoys.

Both the numerical and experimental results demonstrate that the IDWEC performs excellently under random waves, showing promising potential for providing power to deep-sea buoys. Considering that the optimal spring stiffness and PTO damping vary with wave conditions, the development of advanced intelligent controllers to automatically adjust these parameters in response to changing sea states—thereby improving the IDWEC's daily average power generation—will be a primary focus of future research.

CRediT authorship contribution statement

Xiongbo Zheng: Writing – review & editing, Supervision, Funding acquisition, Data curation. **Wenbin Lai:** Writing – original draft, Software, Resources, Methodology. **Jialong Li:** Software, Investigation, Conceptualization. **Fengmei Jing:** Visualization, Investigation, Conceptualization. **Sizhang Rong:** Software, Resources. **Lin Cui:** Visualization, Investigation, Conceptualization. **Hongkun Yang:** Methodology, Investigation.

Declaration of competing interest

The authors declare that they have no known competing financial interests or personal relationships that could have appeared to influence the work reported in this paper.

Acknowledgements

The authors acknowledge the support of the National Nature Science Foundation of China (grant No 52071094).

References

Aguzzi, J., Chatzievangelou, D., Marini, S., et al., 2019. New high-tech flexible networks for the monitoring of deep-sea ecosystems. Environ. Sci. Technol. 53 (12), 6616–6631.

Astariz, S., Iglesias, G., 2015. The economics of wave energy: a review. Renew. Sustain. Energy Rev. 45, 397–408.

Azam, A., Ahmed, A., Yi, M., et al., 2024. Wave energy evolution: knowledge structure, advancements, challenges and future opportunities. Renew. Sustain. Energy Rev. 205, 114880.

Chen, X., Sheng, S., Yang, S., et al., 2025. A novel flexible wave energy converter for concealed power supply to submersible marine buoys: experimental study and mode analysis. Energy 336, 138549.

Cheng, Y., Fu, L., Dai, S., et al., 2022a. Experimental and numerical investigation of WEC-type floating breakwaters: a single-pontoon oscillating buoy and a dual-pontoon oscillating water column. Coast. Eng. 177, 104188.

Cheng, Y., Fu, L., Dai, S., et al., 2022b. Experimental and numerical analysis of a hybrid WEC-breakwater system combining an oscillating water column and an oscillating buoy. Renew. Sustain. Energy Rev. 169, 112909.

Cheng, Y., Gong, J., Zhang, J., 2024a. Hydrodynamic investigation on a single-point moored offshore cage-wave energy converter hybrid system. Ocean Eng. 299, 116848.

Cheng, Y., Liu, W., Dai, S., et al., 2024b. Wave energy conversion by multi-mode exciting wave energy converters arrayed around a floating platform. Energy 313, 133621.

Cordonnier, J., Gorintin, F., De Cagny, A., et al., 2015. SEAREV: case study of the development of a wave energy converter. Renew. Energy 80, 40–52.

Danovaro, R., Fanelli, E., Aguzzi, J., et al., 2020. Ecological variables for developing a global deep-ocean monitoring and conservation strategy. Nat. Ecol. Evol. 4 (2), 181–192.

Deng, F., Wang, J., Wang, J., 2023. Estimation of a five-parameter JONSWAP spectra with an improved particle swarm optimization. Appl. Ocean Res. 136, 103580.

DeVries, T., 2022. The ocean carbon cycle. Annu Rev. Environ. Resour. 47 (1), 317–341.

Di Lauro, E., Maza, M., Lara, J.L., et al., 2020. Advantages of an innovative vertical breakwater with an overtopping wave energy converter. Coast. Eng. 159, 103713.

Felski, A., Zwolak, K., 2020. The ocean-going autonomous ship—challenges and threats. J. Mar. Sci. Eng. 8 (1), 41.

García, E., Quiles, E., Correcher, A., et al., 2018. Sensor buoy system for monitoring renewable marine energy resources. Sensors 18 (4), 945.

Hein, J.R., Koschinsky, A., Kuhn, T., 2020. Deep-ocean polymetallic nodules as a resource for critical materials. Nat. Rev. Earth Environ. 1 (3), 158–169.

Huang, S., Liu, W., Zhang, C., et al., 2021. Numerical calculation and model experiment of a novel external buoy type wave energy converter for navigation lighted buoys numerical study of a novel wave energy converter. IET Renew. Power Gener. 15 (14), 3385–3394.

Hwang, G.T., Annapureddy, V., Han, J.H., et al., 2016. Self-powered wireless sensor node enabled by an aerosol-deposited PZT flexible energy harvester. Adv. Energy Mater. 6 (13), 1600237.

Isson, T.T., et al., 2020. Evolution of the global carbon cycle and climate regulation on earth. Global. Biogeochem. Cycles. 34 (2), e2018GB006061.

Joe, H., Roh, H., Cho, H., et al., 2017. Development of a flap-type mooring-less wave energy harvesting system for sensor buoy. Energy 133, 851–863.

Lai, W., Li, J., Rong, S., et al., 2025. Research on the performance optimization of a hydraulic PTO system for a "Dolphin 1" oscillating-body wave energy converter. China Ocean Eng. 39 (1), 166–178.

Martínez, M.L., Vázquez, G., Pérez-Maqueo, O., et al., 2021. A systemic view of potential environmental impacts of ocean energy production. Renew. Sustain. Energy Rev. 149, 111332.

Pan, P., Sun, Y., Yuan, C., et al., 2021. Research progress on ship power systems integrated with new energy sources: a review. Renew. Sustain. Energy Rev. 144, 111048.

Shi, Q., Wang, H., Wu, H., et al., 2017. Self-powered triboelectric nanogenerator buoy ball for applications ranging from environment monitoring to water wave energy farm. Nano Energy 40, 203–213.

Thiruvenkatasamy, K., Neelamani, S., 1997. On the efficiency of wave energy caissons in array. Appl. Ocean Res. 19 (1), 61–72.

Wang, H., Wu, W., Cui, L., et al., 2022. A new wave energy converter for marine data buoy. IEEE Transac. Industr. Electr. 70 (2), 2076–2084.

Wang, J., Wang, Z., Wang, Y., et al., 2016. Current situation and trend of marine data buoy and monitoring network technology of China. Acta Oceanol. Sin 35 (2), 1–10.

Wang, X., Niu, S., Yin, Y., et al., 2015. Triboelectric nanogenerator based on fully enclosed rolling spherical structure for harvesting low-frequency water wave energy. Adv. Energy Mater. 5 (24), 1501467.

Wang, Y.L, 2015. Design of a cylindrical buoy for a wave energy converter. Ocean Eng. 108, 350–355.

Wen, Z., Guo, H., Zi, Y., et al., 2016. Harvesting broad frequency band blue energy by a triboelectric–electromagnetic hybrid nanogenerator. ACS. Nano 10 (7), 6526–6534.

Wu, N., Wang, Q., Xie, X.D, 2015. Ocean wave energy harvesting with a piezoelectric coupled buoy structure. Appl. Ocean Res. 50, 110–118.

Xi, F., Pang, Y., Liu, G., et al., 2019. Self-powered intelligent buoy system by water wave energy for sustainable and autonomous wireless sensing and data transmission. Nano Energy 61, 1–9.

Xu, R., Wang, H., Xi, Z., et al., 2022. Recent progress on wave energy marine buoys. J. Mar. Sci. Eng. 10 (5), 566.

Yue, W., Wang, K., Jiang, J., et al., 2025. Hydrodynamic performance and structural response of a Sharp Eagle wave energy converter platform under extreme sea states. China Ocean Eng. 39 (2), 373–382.

Zheng, C.W., Wang, Q., Li, C.Y, 2017. An overview of medium-to long-term predictions of global wave energy resources. Renew. Sustain. Energy Rev. 79, 1492–1502.

Zheng, S., Antonini, A., Zhang, Y., et al., 2020. Hydrodynamic performance of a multi-oscillating water column (OWC) platform. Appl. Ocean Res. 99, 102168.

Zheng, X., Ji, M., Jing, F., et al., 2022. Sea trial test on offshore integration of an oscillating buoy wave energy device and floating breakwater. Energy Convers. Manage 256, 115375.

Zhivkoplias, E., Jouffray, J.B., Dunshirn, P., et al., 2024. Growing prominence of deep-sea life in marine bioprospecting. Nat. Sustain. 7 (8), 1027–1037.